

**UNCLASSIFIED**

**AD 4 2 1 7 3 9**

**DEFENSE DOCUMENTATION CENTER**

**FOR**

**SCIENTIFIC AND TECHNICAL INFORMATION**

**CAMERON STATION, ALEXANDRIA, VIRGINIA**



**UNCLASSIFIED**

NOTICE: When government or other drawings, specifications or other data are used for any purpose other than in connection with a definitely related government procurement operation, the U. S. Government thereby incurs no responsibility, nor any obligation whatsoever; and the fact that the Government may have formulated, furnished, or in any way supplied the said drawings, specifications, or other data is not to be regarded by implication or otherwise as in any manner licensing the holder or any other person or corporation, or conveying any rights or permission to manufacture, use or sell any patented invention that may in any way be related thereto.

CATALOGED BY DDC 421739

AS AD No.

ADVANCED FUNCTIONAL ELECTRONIC  
BLOCK DEVELOPMENT

J. R. Biard

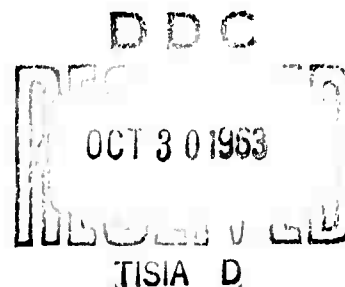
Texas Instruments Incorporated  
Semiconductor-Components Division  
Dallas, Texas

Interim Engineering Report No. 03-63-12

This report covers work done from 15 August 1962 to 15 November 1962.

Contract No. AF33(657)-9824  
Project No. 4159 Task No. 415906

15 May 1963



ADVANCED FUNCTIONAL ELECTRONIC  
BLOCK DEVELOPMENT

J. R. Biard

Texas Instruments Incorporated  
Semiconductor-Components Division  
Dallas, Texas

Interim Engineering Report No. 03-63-12

This report covers work done from 15 August 1962 to 15 November 1962.

Contract No. AF33(657)-9824  
Project No. 4159      Task No. 415906

15 May 1963

Distribution Notice: See WWRN-61-5, 14 July 1960

The basic or applied research reported in this document has been made possible through support and sponsorship extended by the Director of Avionics, Aeronautical Systems Division, under Contract Nr. AF33(657)-9824. It is published for technical information only, and does not necessarily represent recommendations or conclusions of the sponsoring agency.

## TABLE OF CONTENTS

Section	Title	Page
I	TASK I—GaAs EMISSION TECHNOLOGY . . . . .	1
A.	Introduction . . . . .	1
B.	Spontaneous Infrared Emission . . . . .	1
1.	Radiative Recombination Processes . . . . .	1
2.	Device Fabrication . . . . .	7
3.	Efficiency Calculations . . . . .	11
4.	Device Characterization . . . . .	14
C.	Coherent Infrared Emission . . . . .	30
1.	Introduction . . . . .	30
2.	Stimulated Recombination Mechanism . . . . .	31
3.	Laser Geometry and Fabrication . . . . .	31
4.	Laser Performance . . . . .	31
D.	Plans . . . . .	34
II	TASK II—LIGHT MULTIPLEXING . . . . .	35
A.	Introduction . . . . .	35
B.	Optical Design Considerations . . . . .	35
1.	Transmission Efficiency . . . . .	35
2.	Hemispherical Domes . . . . .	35
C.	Coupling Media . . . . .	37
D.	Experimental Results . . . . .	38
E.	Plans . . . . .	38
III	TASK III—ACOUSTIC AMPLIFICATION . . . . .	39
A.	Introduction . . . . .	39
B.	Test Facility . . . . .	39
C.	Fabrication of Ultrasonic Amplifier . . . . .	40
1.	Geometrical Design . . . . .	40
2.	Sample Preparation . . . . .	41
3.	Bonds and Contacts . . . . .	42
D.	Test Results Obtained From Ultrasonic Amplifier Samples . . . . .	43
1.	Samples of Cylindrical Geometry . . . . .	43
2.	Samples With Improved Geometry . . . . .	44
E.	Conclusion and Recommendations . . . . .	47
IV	TASK IV—THERMAL OSCILLATOR . . . . .	49
A.	Objectives . . . . .	49
B.	Analysis . . . . .	49
C.	Plans . . . . .	53
	BIBLIOGRAPHY . . . . .	55

## LIST OF ILLUSTRATIONS

Figure	Title	Page
1	Infrared Output Versus Forward Voltage. . . . .	3
2	Forward Current Versus Forward Voltage . . . . .	5
3	Infrared Output Versus Forward Current . . . . .	6
4	Mesa Diode Infrared Photograph . . . . .	8
5	Flat Geometry Infrared Source . . . . .	9
6	Dome Geometry Infrared Source . . . . .	10
7	Total Internal Reflection in Flat Geometry . . . . .	11
8	Power and Quantum Efficiency Versus Temperature . . . . .	13
9	Infrared Output Versus Slit Width . . . . .	16
10	Calorimeter Used for Diode Efficiency Measurements. . . . .	17
11	Diode Mount for Calorimeter . . . . .	18
12	Radiated Power Versus Forward Current . . . . .	19
13	Quantum Efficiency Versus Temperature . . . . .	20
14	Typical Spectral Distribution . . . . .	21
15	Spectral Distribution With Negligible Low-Energy Radiation. . . . .	22
16	Spectral Distribution of Typical and Manganese Compensated Devices. . . . .	23
17	Spectral Distribution With Modified Diffusion Process. . . . .	25
18	Spectral Distribution Showing Saturation Effects. . . . .	26
19	Diode Equivalent Circuit . . . . .	28
20	Schematic of Modulation Test Equipment. . . . .	28
21	Radiation Intensity Pattern for the Flat Geometry. . . . .	30
22	Laser Geometry and Fabrication. . . . .	31
23	Laser Output Versus Excitation Current . . . . .	32
24	Expanded Scale Laser Output Versus Excitation Current . . . . .	33
25	Cross Section of Hemispherical Structure. . . . .	36
26	Cross Section of Weierstrass Sphere . . . . .	36
27	Block Diagram of Test Facility. . . . .	39
28	Ultrasonic Amplifier . . . . .	40
29	Ultrasonic Amplifier . . . . .	41
30	Ultrasonic Amplifier . . . . .	42
31	Observed Output for Propagation of 10-MC Extensional Waves Along C-Axis of CdS Versus Drift Field . . . . .	44
32	Increase in the Attenuation of CdS Crystal No. 4 to 40-MC Extensional Waves Propagated Along the C-Axis Versus Resistivity. . . . .	46
33	Integrated Circuit Low-Frequency Oscillator . . . . .	50
34	Geometrical Configurations for Thermal Element. . . . .	51
35	Attenuation Versus Normalized Distance. . . . .	52
36	Phase Shift Versus Normalized Distance. . . . .	54

## LIST OF TABLES

Table	Title	Page
I	Radiative Recombination Mechanisms in GaAs . . . . .	2
II	GaAs Spontaneous Emission Peaks. . . . .	24
III	Spontaneous Emission Spectral Characteristics . . . . .	27
IV	Comparison of Acoustic Impedance of CdS, Indium and Fused Silica . . . . .	43
V	Heat Treatment of CdS Crystals . . . . .	45

## ABSTRACT

This report describes investigations of new semiconductor phenomena for application in Advanced Functional Electronic Blocks. The work is divided into four specific tasks; the first two relate to optical phenomena, the third to piezoelectricity, and the fourth to thermal effects. A brief summary by task follows.

### Task I. GaAs Emission Technology

The purpose of this task is to improve the understanding of radiative recombination mechanisms in GaAs P-N junctions and to improve the overall efficiency of these devices as light emitters. This report describes the optical and electrical characteristics of both spontaneous emission sources and lasers. A discussion of the possible radiative recombination mechanisms is also included.

### Task II. Light Multiplexing

A multiplex network or low-level photochopper has been selected as the first application of the GaAs infrared source to FEB's. This report describes geometrical and optical techniques which may be employed to optimize the optical coupling between the GaAs light source and silicon photodetector.

### Task III. Acoustic Amplifier

This task is an exploratory investigation of the ultrasonic amplification effect in piezoelectric semiconductors. This report includes a description of the test facility, fabrication technique, and the results of experiments on the cadmium sulfide amplifiers.

### Task IV. Thermal Oscillator

The defined task in the area of thermal effects relates to the design and fabrication of a thermal low-frequency oscillator in semiconductor network form. This report is primarily concerned with calculations of the thermal characteristics of several promising geometrical shapes.



## FOREWORD

This report was prepared by the Semiconductor-Components Division of Texas Instruments Incorporated, Dallas, Texas, on Air Force Contract AF 33(657)-9824 under Task No. 415906 of Project No. 4159, "Advanced Functional Electronic Block Development." The work is administered under the direction of Electronic Technology Laboratory, Aeronautical Systems Division. William Spaid is the project engineer for the Laboratory.

The studies presented began in August 1962, and are still in process. The work is under the direction of J. S. Kilby, Manager of Integrated Circuits Engineering. Charles Phipps is the Program Manager.

The work described was a group effort under the technical supervision of Dr. J. R. Biard.

This report is the First Interim Report on Contract AF 33(657)-9824 and covers work from 15 August 1962 to 1 December 1962. The contractors report number is 03-63-12.

This report is unclassified.

TEXAS INSTRUMENTS INCORPORATED  
Semiconductor-Components Division  
Dallas, Texas

15 May 1963

ADVANCED FUNCTIONAL ELECTRONIC  
BLOCK DEVELOPMENT

03-62-12

SECTION I

TASK I. - GaAs EMISSION TECHNOLOGY

A. INTRODUCTION

The purpose of this task is to improve the understanding of radiative recombination mechanisms in GaAs P-N junctions and to improve the overall efficiency of these devices as light emitters.

The problems presented by this task cover device technology and the evaluation of the infrared emission characteristics of GaAs junctions. This investigation will emphasize design limits as required to adequately define future tasks relating to FEB's based on infrared coupling. A task of this type is necessary if the vast potential offered by the GaAs IR source is to be properly exploited in FEB's.

B. SPONTANEOUS INFRARED EMISSION

1. Radiative Recombination Processes

The energy band structure of GaAs is particularly favorable for obtaining the radiative recombination processes desired for a highly efficient infrared source. The principal energy band extremes are located at the same point (0, 0, 0) in k-space and radiative recombination may occur without the exchange of momentum and energy with the lattice as required in germanium and silicon. The Auger (3-body) recombination process which does not result in photon generation<sup>1</sup> should not be important in GaAs due to the relatively large bandgap of the material. Recombination via impurity centers, generally deep lying, in which one or more lattice phonons are captured or emitted is thought to be the dominant nonradiative process in GaAs.

---

<sup>1</sup> Numerals denote references listed at end of text.

Radiative recombination in GaAs may occur through at least four different processes:

Direct band-to-band

Neutralization of a compensating or ionized impurity center

Decay of unbound excitons

Decay of bound excitons.

These processes are summarized in Table I for transitions involving both acceptors and donors, where  $\ominus$  and  $\oplus$  denote ionized acceptors and donors respectively. The direct band-to-band recombination mechanism<sup>1</sup> has not been isolated as an important source of radiation in GaAs infrared diodes. Processes (b) and (c) are thought to be the dominant radiative processes in GaAs for spontaneous emission.

Neutralization of a compensating acceptor center, process (b), may be expected to occur with hole injection into N-type material. Process (b) may also occur in P-type material with deep lying acceptors and injected electrons. The photoluminescent spectrum of GaAs bulk material doped with zinc acceptors shows emission at an energy somewhat less than the bandgap of GaAs<sup>2</sup> and corresponds in energy to emission from zinc-doped GaAs junctions. In addition, sources obtained by diffusing zinc into N-type material compensated with manganese show strong radiation lines consistent with recombination via both the zinc and the deeper lying acceptor, manganese (see radiation spectrum, part B4, b).<sup>3</sup> Strong radiative recombination via donor levels, process (c), and exciton recombinations, processes (d), (e), and (f) have not been defined by experiment in GaAs junction sources to date (Table I).

Table I. Radiative Recombination Mechanisms in GaAs

Designation	Description	Symbolic Representation
(a)	Direct band-to-band	$+ \text{ and } - \rightarrow \sim$
(b)	Via neutral acceptor	$\ominus + \text{ and } - \rightarrow \ominus \text{ and } \sim$
(c)	Via neutral donor	$\oplus - \text{ and } + \rightarrow \oplus \text{ and } \sim$
(d)	Unbound exciton	$+ - \rightarrow \sim$
(e)	Bound exciton	$\oplus - \text{ and } + - \rightarrow \oplus^- + \rightarrow \oplus - \text{ and } \sim$
(f)	Bound exciton	$\ominus + \text{ and } - + \rightarrow \ominus^+ - \rightarrow \ominus + \text{ and } \sim$

Additional information concerning recombination mechanisms has been obtained from an analysis of the diode V-I characteristic and the dependence of photon density  $N_0$  on diode voltage and current. The integrated photon flux  $N_0$  as shown in Figure 1 as a function of terminal voltage bias  $V$  for several temperature values is described by Equation (1).

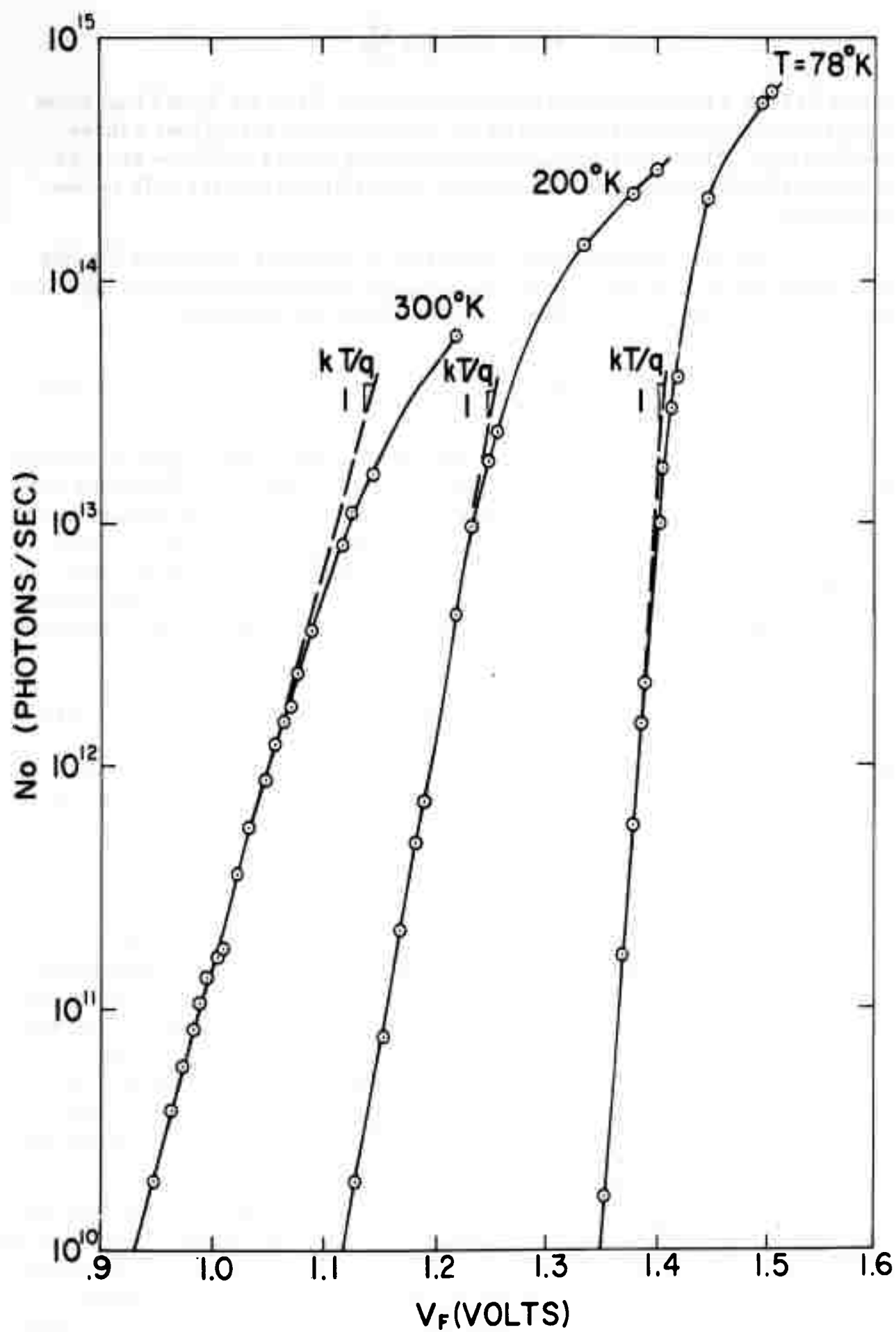


Figure 1. Infrared Output Versus Forward Voltage

$$N_0 = U(T) \exp \frac{qV}{kT} \quad (1)$$

where  $U(T)$  is a temperature dependent prefactor. Here the dotted line slope  $kT/q$  from Equation (1) is seen to fit the observed data throughout a three-decade range. The larger voltage drop appearing across the diode sources at high forward current may be explained as resulting from the bulk series resistance.

The terminal V-I characteristics of the GaAs units used for this investigation are characterized by two principal current components, specifically " $kT$ " and " $nkT$ " components, as indicated by Equation (2).

$$I = A(T) \exp \frac{qV}{kT} + B(T) \exp \frac{qV}{nkT} \quad (2)$$

where  $A(T)$  and  $B(T)$  are temperature dependent coefficients. The V-I characteristic of the diode used in Figure 1 is presented in Figure 2. The diode current is seen to be dominated by the " $kT$ " and " $nkT$ " components at sufficiently large and small current values respectively. The departure from the " $kT$ " asymptote at high current is again due to the voltage drop across the bulk series resistance. Based on the characteristics of Figures 1 and 2 the photon flux,  $N_0$ , should vary directly as the device current at large current densities as in Equation (3).

$$N_0 = D(T) I \quad (3)$$

where  $D(T)$  is a temperature dependent factor. Similarly, at sufficiently small current values it follows from Equations (1) and (2) that  $N_0$  varies as  $I^n$  as in Equation (4).

$$N_0 = E(T) I^n \quad (4)$$

where  $E(T)$  is a temperature dependent factor. The experimental data of Figure 3 where  $N_0$  is plotted against current  $I$  does approach the asymptotic slopes of  $I$  and  $n$  at large and small current densities as expected from Equations (3) and (4). Data is shown in Figure 3 for 78° and 300° Kelvin; note that the values of  $n$  are the same in Figures 2 and 3. The current which varies as  $\exp(qV/nkT)$  is the recombination current described stastically by Sah, Noyce, and Shockley<sup>4</sup> and is due to recombination via centers located near the center of the bandgap. In GaAs the " $nkT$ " current is known to be sensitive to the conditions at the device surface.

Recent work by Coppen and Matzen<sup>5</sup> concludes for silicon that the electron flow associated with the " $kT$ " current component is distributed throughout the area of the junction, but that the " $nkT$ " current is concentrated at the junction periphery. The above observations support the same conclusion for GaAs, i. e., that the infrared radiation is derived from the bulk " $kT$ " current component and that the " $nkT$ " component of current is concentrated at the

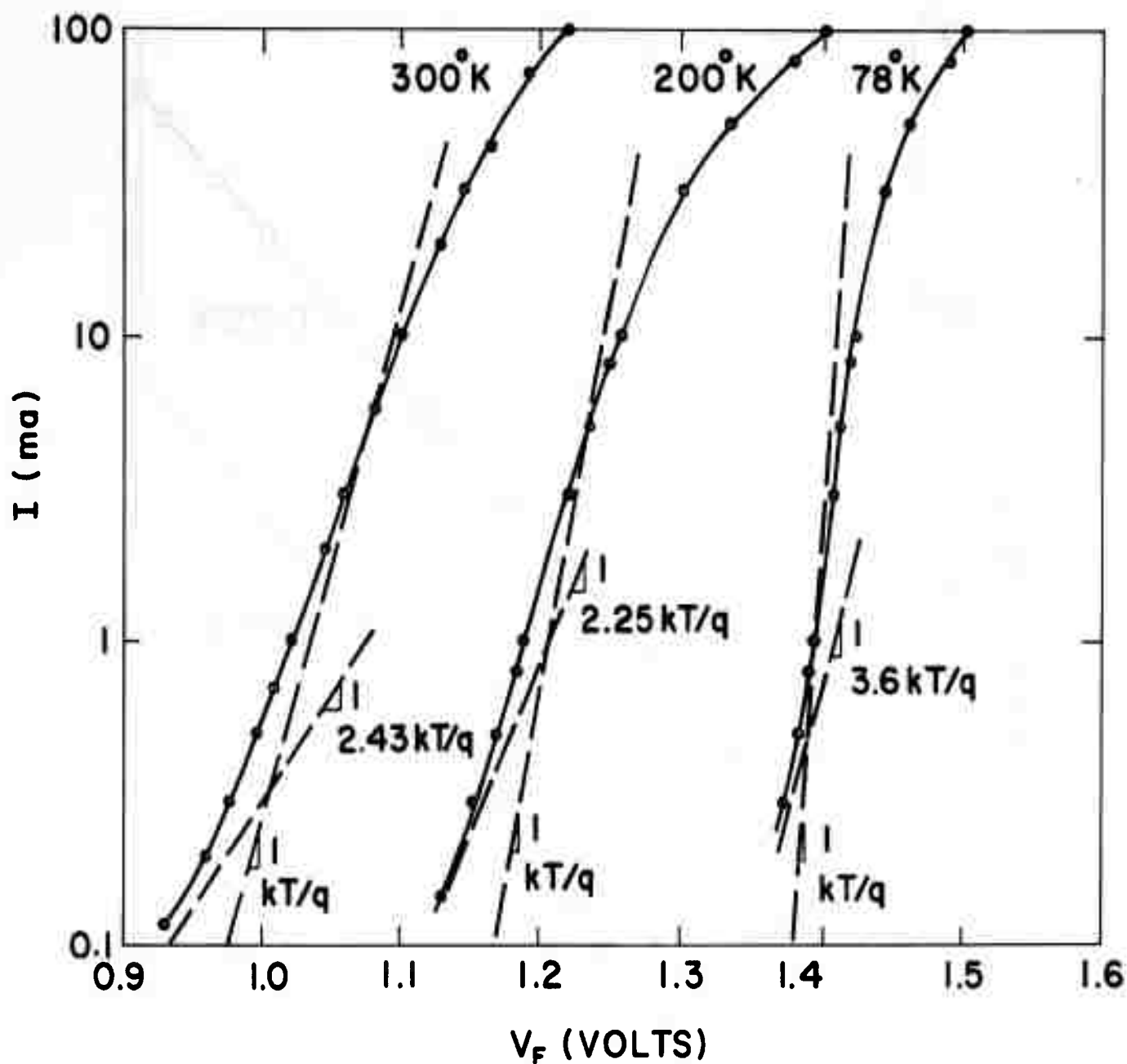


Figure 2. Forward Current Versus Forward Voltage

junction periphery. An inspection of the infrared emission at the periphery of the radiating junctions has revealed no photon flux that might be associated with the " $nkT$ " current flow in this region for GaAs.

An experiment was performed to check for the presence of band-edge (0.9 micron) radiation from the bulk of the N-type GaAs in an IR source. It was felt that such radiation might be present due to absorption and subsequent reradiation of photons generated near the P-N junction. The presence of this mechanism could result in a significant increase in external quantum efficiency since rays which are normally internally reflected could ultimately be emitted through absorption and reradiation.

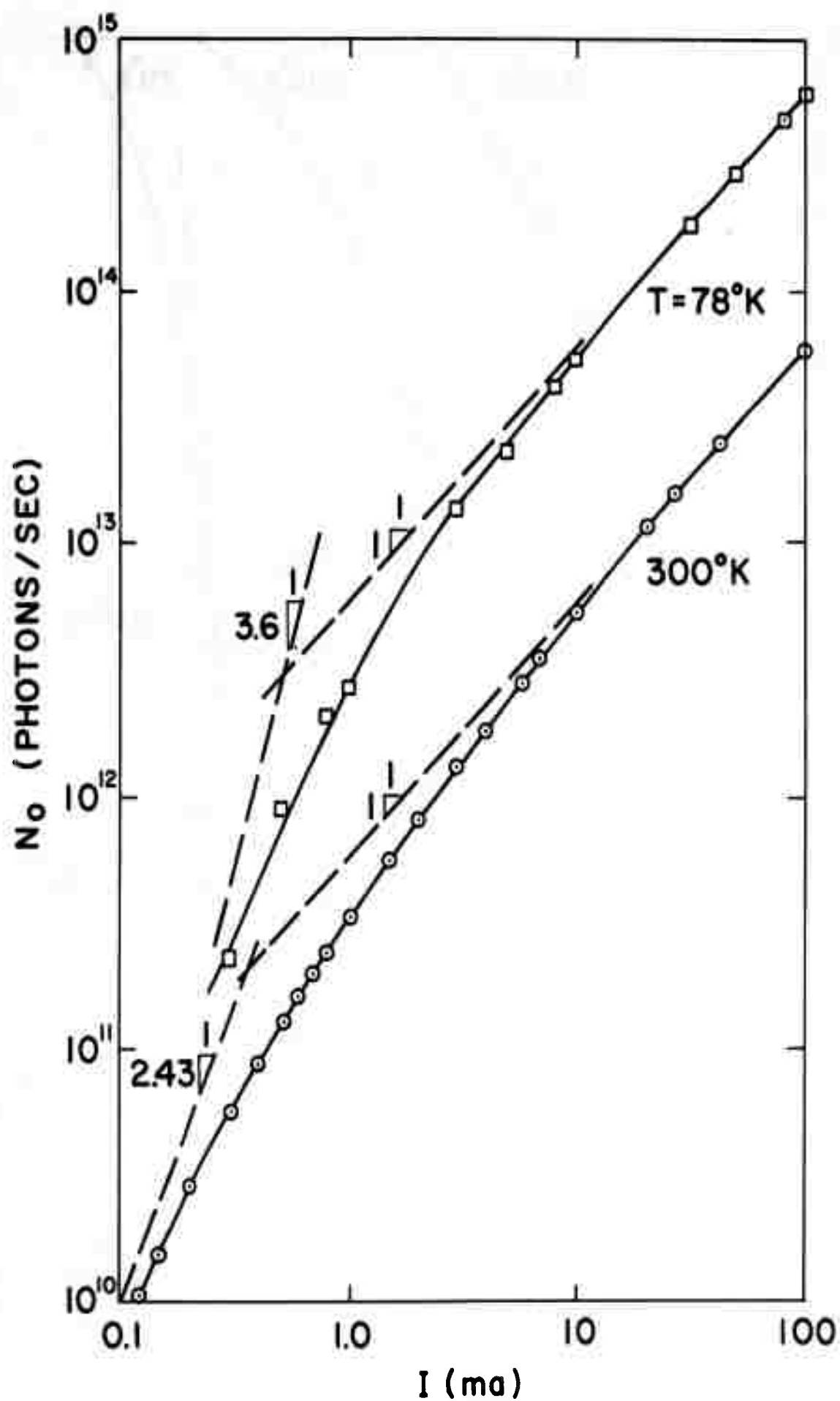


Figure 3. Infrared Output Versus Forward Current

The diode used in the test was formed in the following manner: A mesa approximately 15 mils in diameter was etched from the P-layer on a square wafer 50 mils on a side. The unit was mounted on a tab with the mesa positioned over a hole, the outline of which is visible in the photograph of Figure 4. The photograph was made with the infrared radiation from the diode. The mesa is on the underside of the unit as viewed in the photograph. The absorption coefficient is small, as evidenced by the radiation emerging from the edges of the wafer, in some places as much as 30 mils from the edge of the junction. The experiment consisted of forming an infrared image of the forward-biased GaAs mesa diode and probing that image with a silicon phototransistor as the temperature of the GaAs diode was changed from 300° K to 77° K. In all cases significant 0.9-micron radiation was found only in the area covered by the mesa. From this result it was concluded that for present GaAs diodes a negligible amount of the observed infrared is contributed by absorption and reradiation in the N-type bulk. This experiment will be repeated periodically as changes are made in the material and fabrication processes of the GaAs infrared source.

Various observed characteristics of the radiative recombination process in zinc diffused GaAs diodes may be summarized as follows:

Bulk effect

Follows  $\exp(qV/kT)$

Photon energy less than bandgap

Involves acceptor impurity level.

These characteristics strongly suggest that the dominant mechanism for Lossev emission in the present diodes is the recombination through compensating acceptor impurity levels of holes injected into the N-type side of the junction. In most cases the compensating acceptor impurities would result from the leading edge of the zinc diffusion profile and would therefore be present only near the P-N junction. This would account for the absence of the characteristic wavelength in photoluminescence experiments on homogenous N-type samples<sup>2</sup> and the absence of significant absorption and reradiation in mesa diodes.

## 2. Device Fabrication

Both flat and dome-shaped device geometries are being investigated, the latter providing the advantage of higher overall external quantum efficiency.

A top view of the flat device is shown in Figure 5(a) and 5(b), using emitted infrared light and visible light, respectively. The visible photograph of the flat device in Figure 5 shows interrelation of the header, wafer and contacts. The junction here was produced by diffusing zinc into an N-type GaAs wafer doped to a concentration  $N_d = 10^{17} \text{ cm}^{-3}$  with tin. Due to the unique characteristics of acceptor diffusion in GaAs, this process results in a  $P^+ - N$  abrupt junction. The junction of this device is in a plane parallel to the surface





Figure 4. Mesa Diode Infrared Photograph

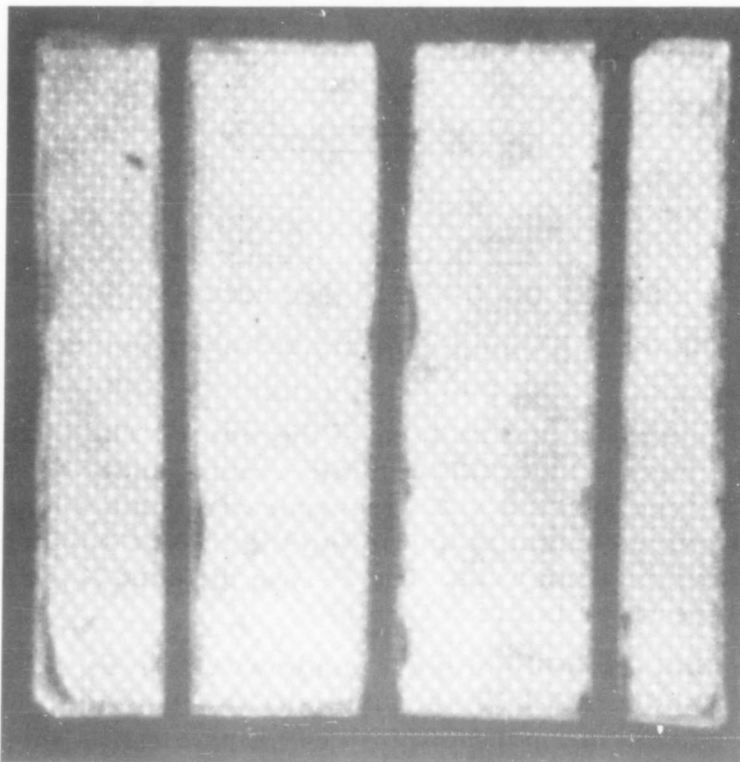
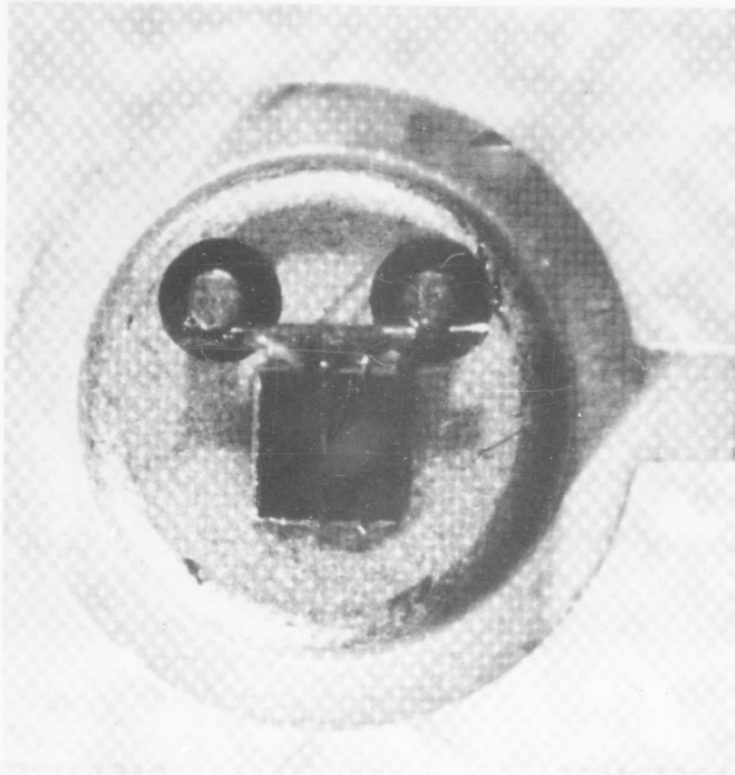


Figure 5. Flat Geometry Infrared Source

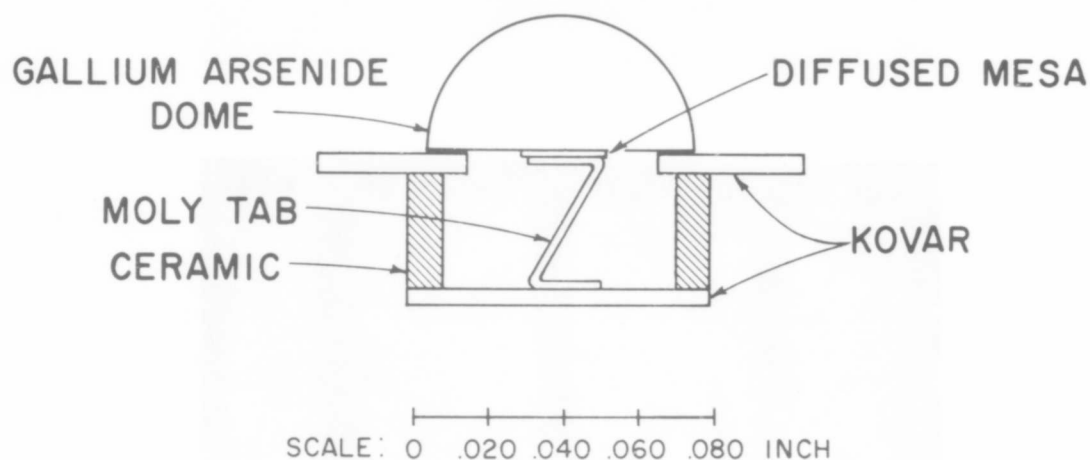
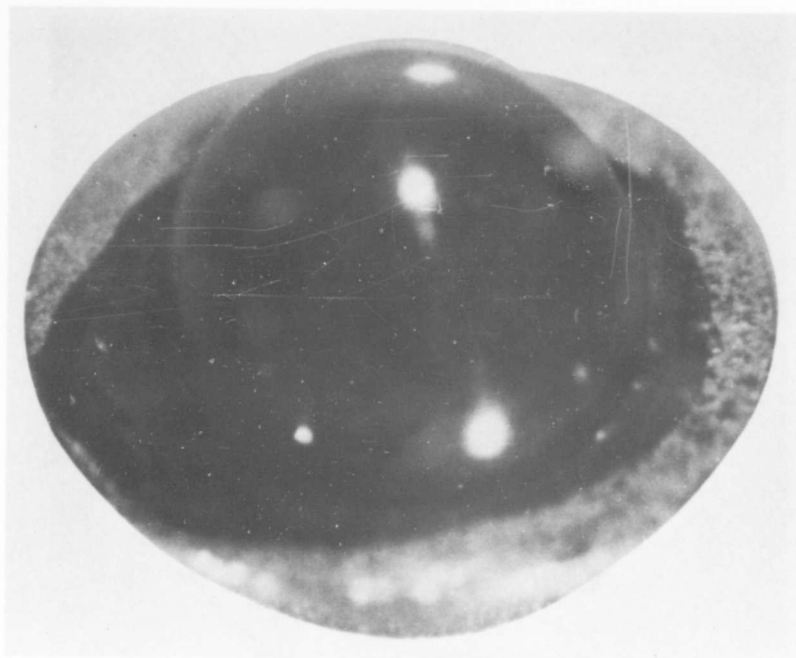


Figure 6. Dome Geometry Infrared Source

of the wafer and covers the entire area of the wafer. The infrared light penetrates through the N-type layer. The ohmic contact under the wafer is obtained by covering the P-type surface with an evaporated contact and soldering to the header. A spaced wire contact is applied to the N-type surface of the wafer using tin-plated molybdenum wire. The P-type diffused layer is about 0.5 mil thick and the N-type layer is 2.5 mil thick.

The dome-shaped units are made with N-type starting material in which zinc is diffused to obtain an abrupt, shallow junction. The resulting material is then ground and polished into hemispherically shaped structures and mounted on a header. A photograph of a polished dome unit mounted in a pill package is shown in Figure 6. The relative efficiencies expected and obtained from these hemispherical units is discussed in Section II.

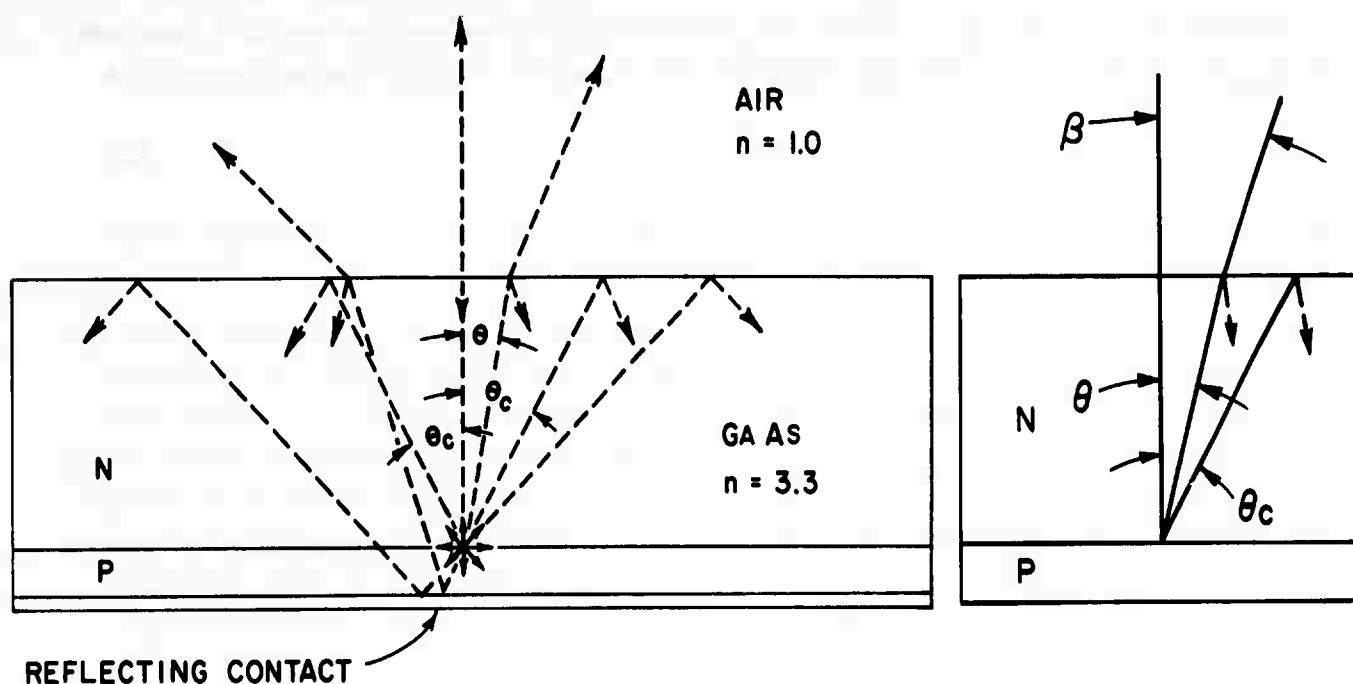


Figure 7. Total Internal Reflection in Flat Geometry

### 3. Efficiency Calculations

For a gallium arsenide-air interface in the planar diode structure, a critical angle for total internal reflection,  $\theta_c$ , exists which is defined as:

$$\theta_c = \sin^{-1}\left(\frac{1}{3.3}\right) \quad (5)$$

where 3.3 is the index of refraction of gallium arsenide;  $\theta_c$  is therefore 17.5 degrees. This means that although a recombination center may be radiating uniformly in all directions, only that radiation which intersects a surface within 17.5 degrees of the normal will be transmitted through the interface. Referring to Figure 7, if we consider only one surface, that of the N-layer, the fraction of the total radiation which will intersect that surface within the critical angle is 0.023, or 2.3 percent. Of this, only 68 percent will be actually transmitted due to reflection losses at the interface, so that 1.57 percent of the radiation generated will be transmitted if bulk absorption is negligible.

However, if we consider a structure in which the P-layer surface is covered with a reflective coating, the radiation intersecting the surface of the P-layer may be reflected back toward the N-layer surface and another 1.57 percent of the radiation could be transmitted. In addition, if both surfaces are sufficiently plane-parallel and bulk absorption is negligible,

multiple reflections will eventually result in 100-percent transmission within the critical angle, so that 4.6 percent of the generated radiation will be transmitted.

Because the radiation which is transmitted through a gallium arsenide-air interface is refracted, the amount of refraction being a function of angle of incidence, the intensity of the radiation varies approximately as

$$I = I_0 \cos \beta \quad (6)$$

where  $I_0$  is the intensity when viewed on the normal and  $\beta$  is the angle from the normal.

To test the hypothesis previously mentioned of reflection from the P-layer, surface diodes were fabricated with both rough and highly polished P-layer surfaces. Diodes with polished surfaces were invariably more efficient than those with rough surfaces, the best polished units being three times more efficient than the average rough-surfaced units. The ratio of the worst and best transmission percentages previously described is also approximately three, so that indirect correlation is obtained. In order to further test the proposed hypothesis, it is proposed that a direct measurement of internal reflectivity be made as a function of surface finish.

Quantum efficiency,  $\eta$ , is defined as number photons/number electrons. The external quantum efficiency,  $\eta_e$ , of the best flat geometry device at room temperature is 0.27 percent. Since the maximum transmission is 4.6 percent, the minimum internal quantum efficiency is:

$$\eta_i \Big|_{300^\circ\text{K}} = \frac{\eta_e}{0.046} = \frac{0.27\%}{0.046} = 5.9\% \quad (7)$$

at 77°K, the best present external quantum efficiency is 2.4 percent, so that:

$$\eta_i \Big|_{77^\circ\text{K}} = \frac{2.4}{0.046} = 52.0\% \quad (8)$$

The various quantum efficiencies discussed above are shown as a function of temperature in Figure 13. Since N- and P-type GaAs are known to absorb the wavelengths of radiation emitted in these diodes, the internal quantum efficiencies indicated in Equations (7) and (8) are low by some unknown factor. It should be understood that these values are lower bounds only; accurate determination of the actual internal quantum efficiency will require a detailed knowledge of the bulk absorption of the N- and P-type layers of GaAs.

The externally measured quantum efficiency  $\eta_e$  and the power efficiency  $\psi_e$  have been compared in Figure 8 for a flat GaAs source. Note that the power efficiency exceeds the quantum efficiency. The larger  $\psi_e$  values are expected in units of low series resistance because the terminal potential across the GaAs source,  $V_f$ , corresponds to an energy value somewhat less than that of the radiated photons,  $E$ .

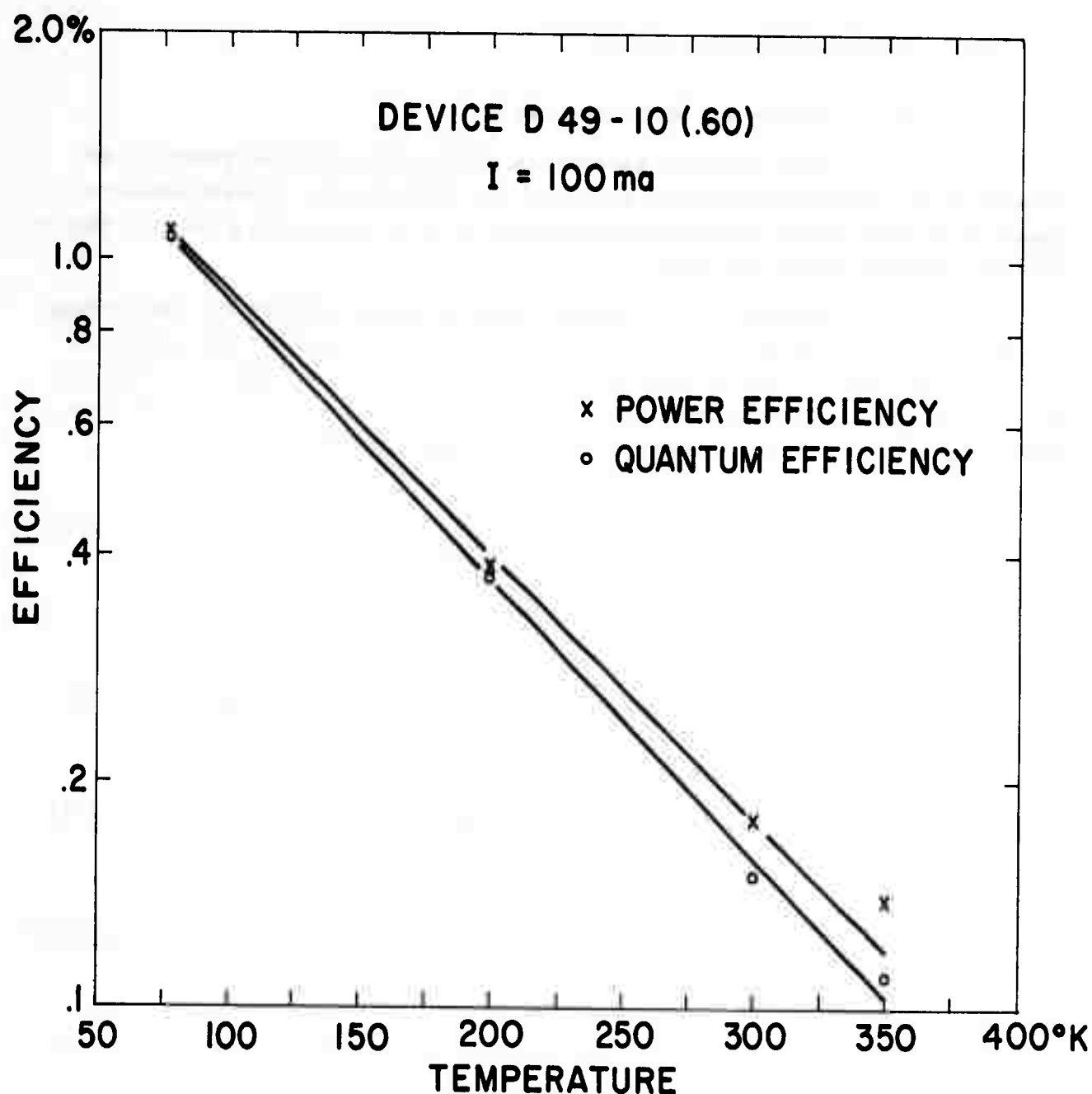


Figure 8. Power and Quantum Efficiency Versus Temperature

The expression relating  $\eta_e$  and  $\psi_e$  is given in Equation (9):

$$\psi_e = \eta_e \frac{E}{V_f} \quad (9)$$

At higher current levels  $V_f$  will become greater than  $E$  and quantum efficiency will be greater than power efficiency. Since  $E$  can be greater than  $V_f$  it has been proposed that the GaAs IR source might produce a net cooling effect; i.e., a value of  $\psi_e$  greater than 1. Based on Equation (9) the observation of net cooling seems unlikely. At room temperature  $E$  is about 13 percent greater than  $V_f$ , but the external quantum efficiency is low; while at liquid nitrogen temperature where the quantum efficiency is high,  $E$  and  $V_f$  are essentially equal.

#### 4. Device Characterization

##### a. Efficiency Measurements

Accurate measurements of the total spectral power available from the GaAs sources are required for FEB design. These measurements have been made using three independent techniques and good correlation between data has been obtained.

One of the techniques uses the spectrometer for measuring the absolute spectral power radiated from the GaAs source at the spectrometer entrance slit. A black body source was made using a Globar heating element. The spectral photon flux distribution of the Globar is calculated from knowledge of the source temperature  $T$  and Equation (10).

$$W_1 = \frac{2\pi}{h^3 c^2} \frac{E^2}{\exp\left(\frac{-E}{kT}\right) - 1} \quad (\text{MKS Units}) \quad (10)$$

where  $E$  is the photon energy.

Similarly, the spectral power distribution supplied by the black body source is given by Equation (11).

$$W_2 = \frac{2\pi}{h^3 c^2} \frac{E^3}{\exp\left(\frac{-E}{kT}\right) - 1} \quad (11)$$

Substituting numerical values into Equations (10) and (11) yields Equations (12) and (13).

$$W_1 = \frac{9.85 \times 10^{22} \text{ V}^2}{\exp\left(\frac{V}{8.62 \times 10^{-5} T}\right) - 1} \left( \frac{\text{Photons}}{\text{cm}^2 \cdot \text{sec} \cdot \text{ev}} \right), \quad (12)$$

$$W_2 = \frac{1.57 \times 10^4 \text{ V}^3}{\exp\left(\frac{V}{8.62 \times 10^{-5} T}\right) - 1} \left( \frac{\text{watts}}{\text{cm}^2 \cdot \text{ev}} \right). \quad (13)$$

where  $V = qE$  is expressed in electron-volts.

Equations (12) and (13) provide values for the spectral flux density from the black body surface in watts/cm<sup>2</sup> · ev and photons/cm<sup>2</sup> · sec · ev as functions of temperature and energy. Direct spectral comparisons of the black body and the GaAs flat source were obtained using identical radiating areas and the same focusing arrangement for each. For this comparison a Perkin-Elmer Model 112U double-pass prism monochrometer with a linear thermocouple detector was used. Although the spectrometer does not collect all of the radiation from the sources, the ratio of the thermocouple responses for black body and GaAs flat source is an accurate measure of the relative intensities because both sources provide a Lambert's law spatial radiation pattern

(see Section B4d Figure 21). The black body temperature  $T$  required for  $W_1$  and  $W_2$  evaluation is obtained by inserting a thermocouple into a 9-mil diameter hole machined into the Global surface. Computer solutions of the  $W$  values as functions of temperature  $T$  and energy  $E$  are used to obtain values for device external quantum efficiency  $\eta_e$  in air, integrated photon flux  $N_o$ , external power efficiency and  $\psi_e$ , and radiated power  $P_o$  as shown by Equations (14), (15), (16), and (17).

$$\eta_e = \frac{2A}{I} \int_0^{\infty} R(E)W_1 dE \quad (14)$$

$$N_o = A \int_0^{\infty} R(E)W_1 dE \quad (15)$$

$$\theta_e = \frac{A}{IV} \int_0^{\infty} R(e)W_2 dE \quad (16)$$

$$P_o = A \int_0^{\infty} R(e)W_2 dE \quad (17)$$

where  $A$  is the radiation area of both the GaAs source and the black body radiator,  $I$  is the current supplied to the GaAs source,  $V$  is the GaAs terminal voltage, and  $R(E)$  is the ratio of the power measured at the thermocouple detector from the GaAs source to that obtained with the reference black body at a photon energy  $E$ .

Equations (14) through (17) may be experimentally evaluated using a graphical integration technique and accurately determined values for  $R(E)$ ,  $A$ ,  $I$ ,  $V$ ,  $W_1$ , and  $W_2$ .

The effect of spectrometer mechanical slit width upon  $R(E)$  and the corresponding  $N_o$  values is illustrated by a sample measurement in Figure 9. No error due to a finite sampling spectral width occurs for slit width  $\Delta_x$  values of less than about 0.5 mm for the unit measured.

A second technique for measuring the radiated spectral power involves a calorimetric measurement comparing radiating and non-radiating forward-biased GaAs sources. A specially designed vacuum calorimeter pictured in Figure 10 is used for this measurement. Here the radiated diode power was measured directly in the calorimeter by comparing values of input power required to maintain a radiative and nonradiative unit at the same temperature.

The units to be compared are mounted as shown in Figure 11 within the evacuated area on a mount of low thermal resistance which is connected by a known thermal resistance to the cold sink. This cold sink is



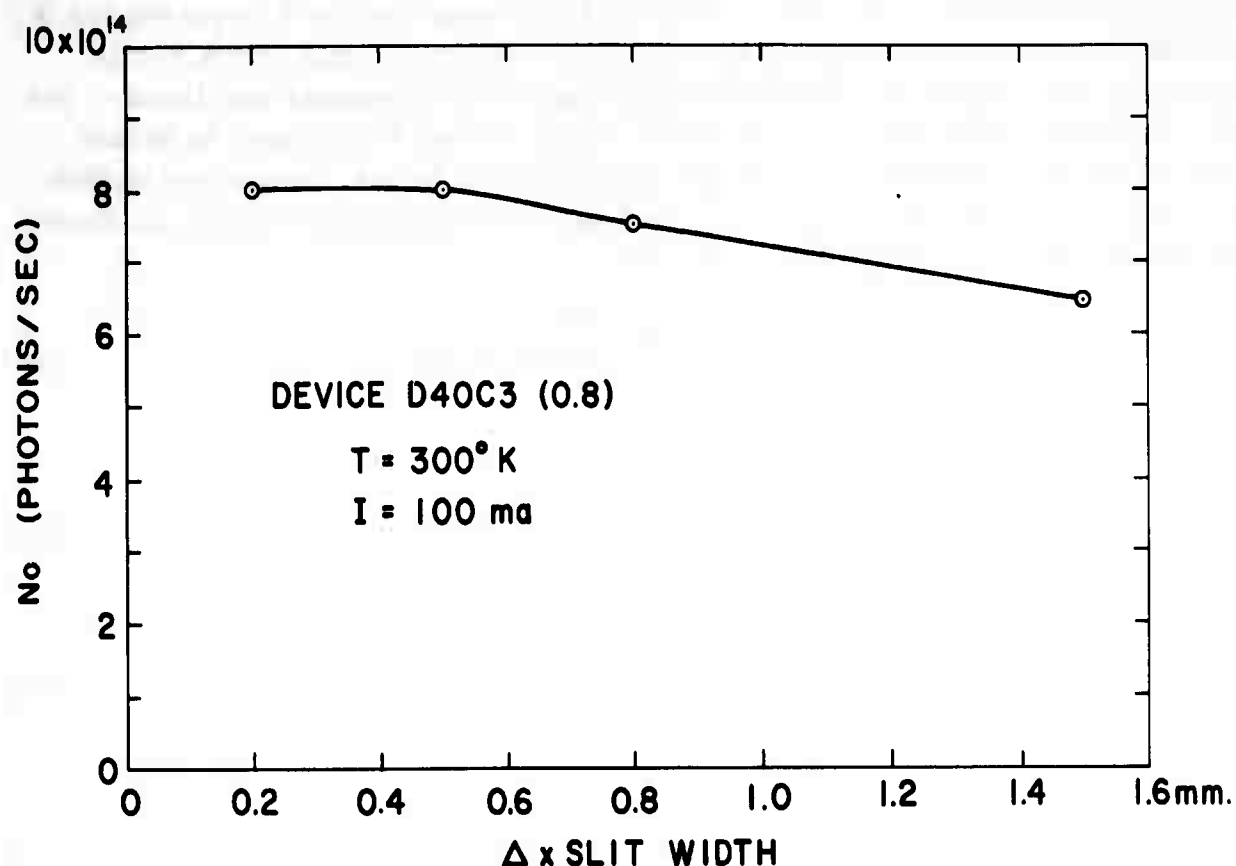


Figure 9. Infrared Output Versus Slit Width

accurately maintained at  $78^{\circ}\text{K}$  by partially filling the stainless steel tube which supports it with liquid nitrogen. As shown in Figure 10 the entire diode mount assembly is surrounded by a copper box which is maintained at liquid nitrogen temperature to shield from external heating by radiation.

During the test, one of the diodes is allowed to radiate its infrared emission into the vacuum while the reference diode is completely surrounded by the mount. Both units are forward biased and the total power dissipated as heat is held constant by accurately maintaining the temperature of the mount; a forward-biased XD500 GaAs Varactor Diode is used as the thermometer. The radiated infrared power is determined from the difference between the power supplied to the radiative and nonradiative sources. It is usually necessary to make a trial run with both infrared sources covered to correct for thermoelectric effects and  $I^2R$  heating in lead wires. Figure 12 shows a plot of radiated power versus current as measured by this technique for a flat geometry GaAs source at  $140^{\circ}\text{K}$ .

A third technique for measuring the infrared radiator uses calibrated energy and photon detectors. The detectors used have been thermocouples, phototubes, gas filled phototubes, photomultiplier tubes, and silicon solar cells. In each case the detector was calibrated by comparison with an Eppley thermopile. This type measurement is the easiest of the three to make and is used most extensively in general laboratory work.



Figure 10. Calorimeter Used for Diode Efficiency Measurements

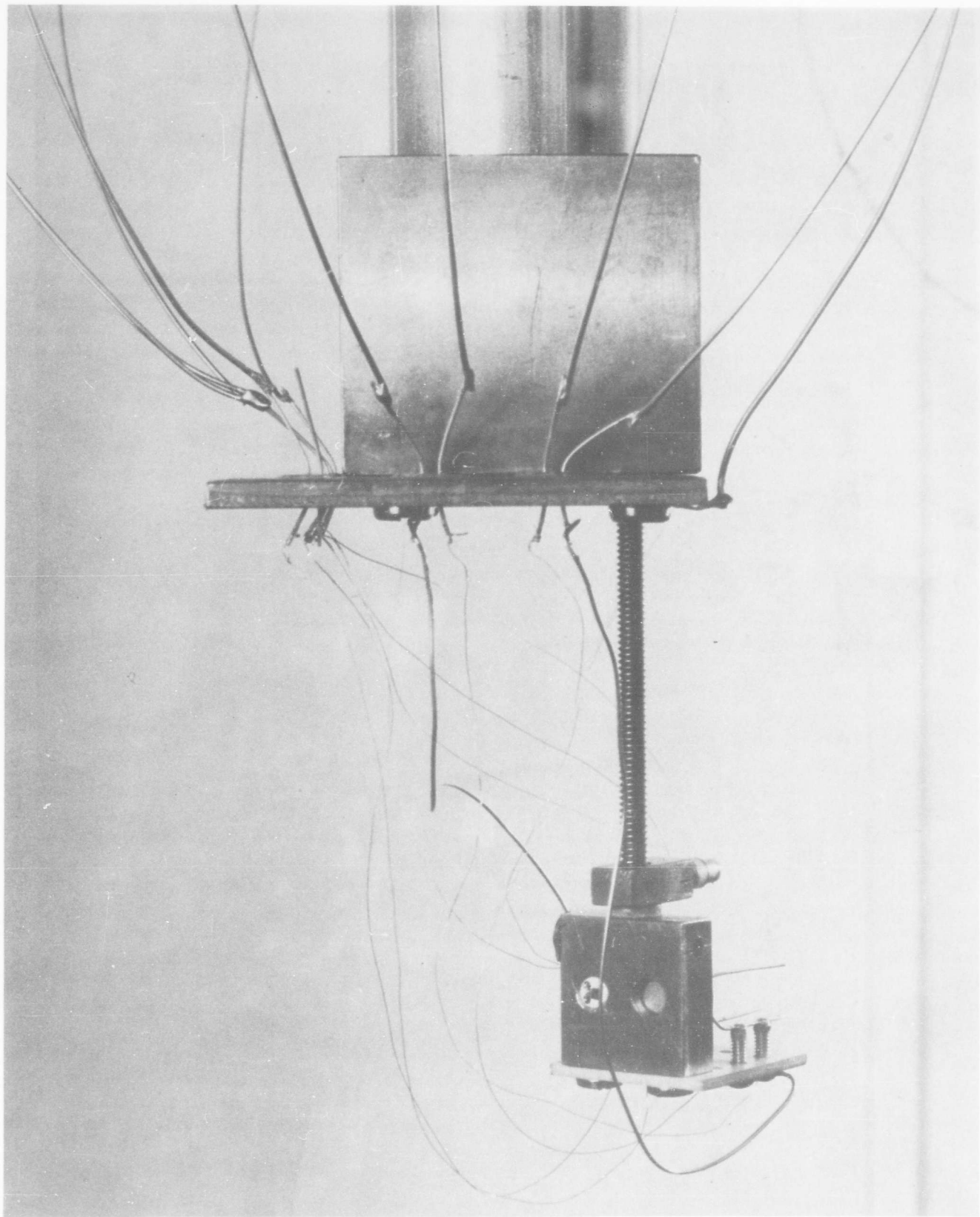


Figure 11. Diode Mount for Calorimeter

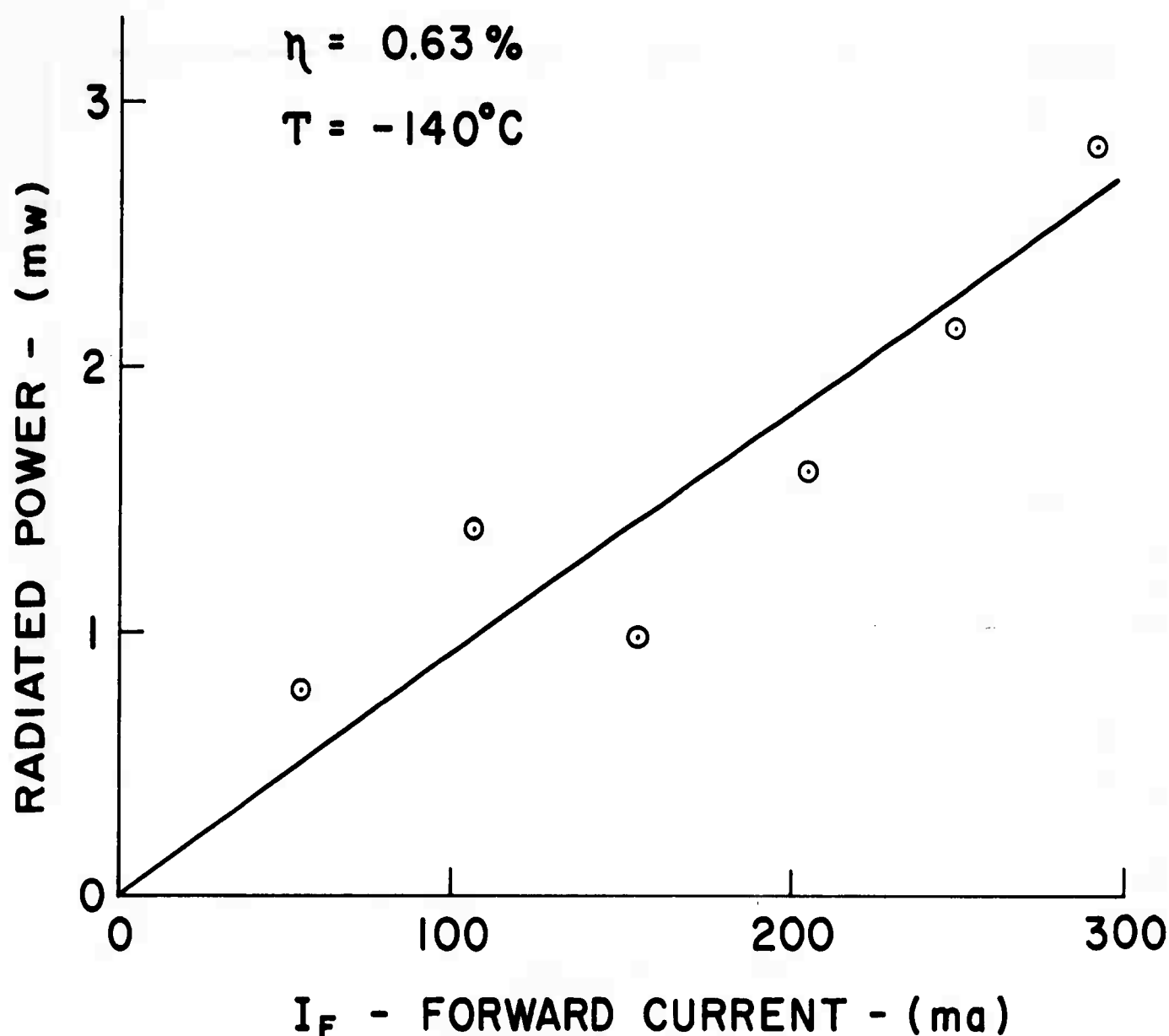


Figure 12. Radiated Power Versus Forward Current

Each of the measuring techniques has been used to obtain the external quantum efficiency  $\eta_e$  values as a function of temperature  $T$  for a typical, flat unit. As indicated in Figure 13, very good correlation between measurement techniques has been achieved.

The expression for  $\eta_e$  quantum efficiency as a function of temperature for the typical uncanned unit of Figure 13 is given approximately by

$$\eta_e = 2.65 \exp(-T/107) \%, \text{ for } T \text{ in } ^\circ\text{K} \quad (18)$$

for the range of temperatures shown. A possible temperature-insensitive region is indicated in the high temperature region. For present GaAs sources, the emission at liquid nitrogen is about a factor of 10 greater than that at room temperature.

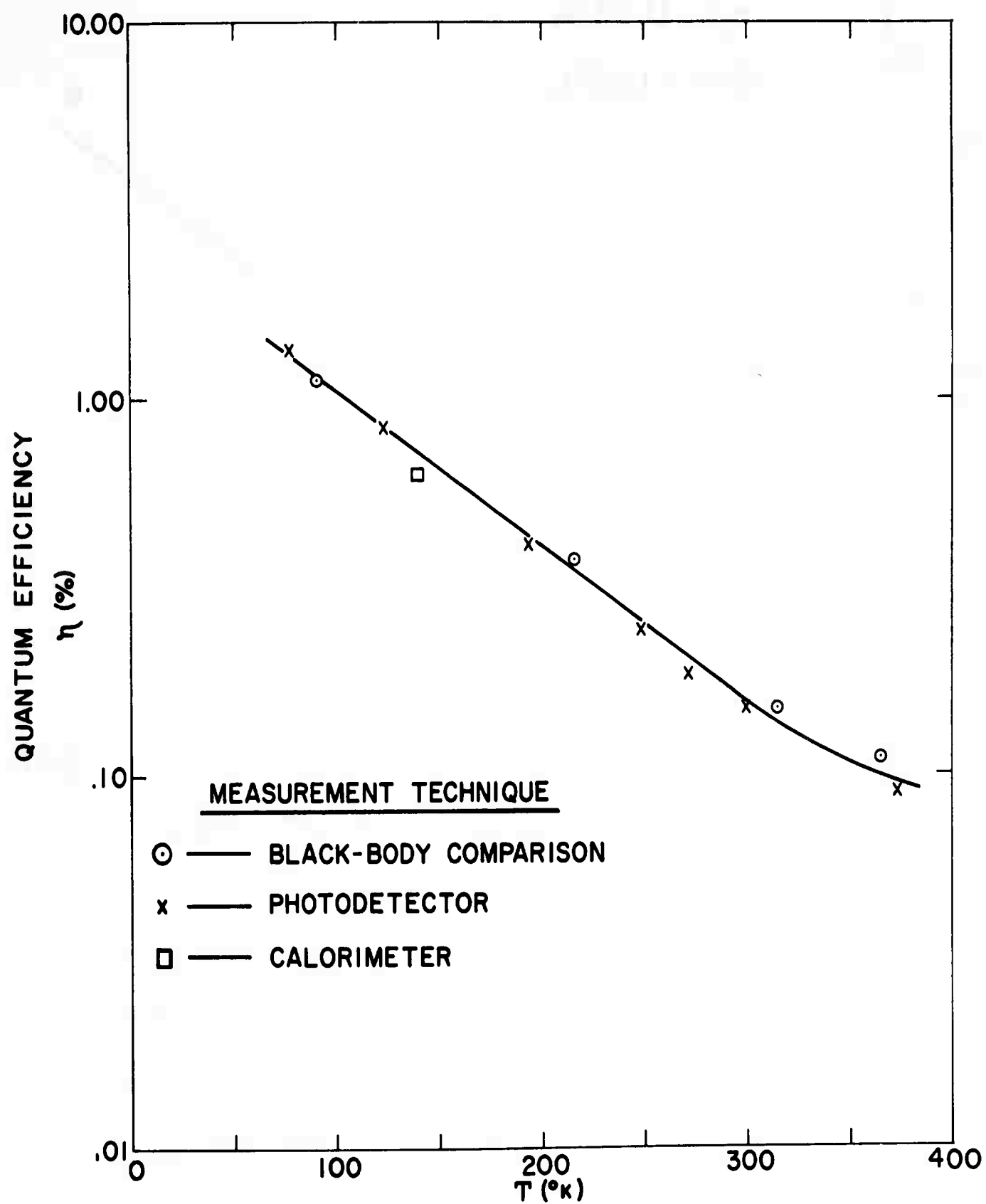


Figure 13. Quantum Efficiency Versus Temperature

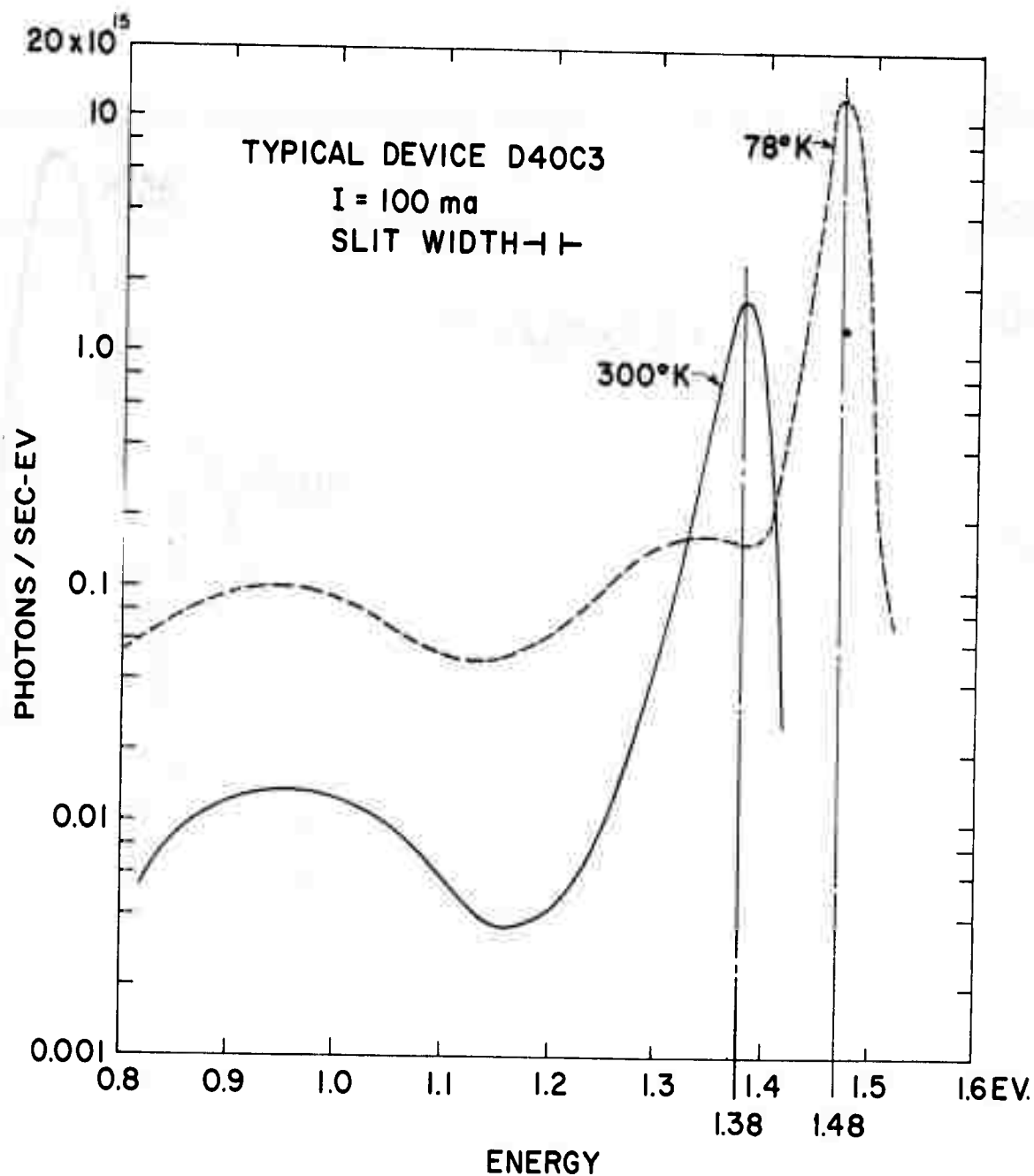


Figure 14. Typical Spectral Distribution

b. Spectral Distribution

Measurements of the radiated photon flux density were made using the Perkin-Elmer 112U spectrometer fitted with a quartz prism and both thermocouple and PbS detectors. Mounts are available for operating the GaAs sources over a temperature range from liquid helium to temperatures above that of boiling water. The photon flux  $\Phi$  measured in photons/sec . ev as a function of energy is shown in Figure 14 for a typical unit operated at low current levels in the spontaneous emission mode. In addition to the primary radiation maximum, one may note additional peaks in the 1.0 and 1.3 ev range. The typical unit shown here is operated at 100 ma and contains a junction area of  $1.6 \times 10^{-2} \text{ cm}^2$ . Note that the photon flux in Figure 14 at the low energy radiation peak is approximately 0.5 percent of the primary maximum.

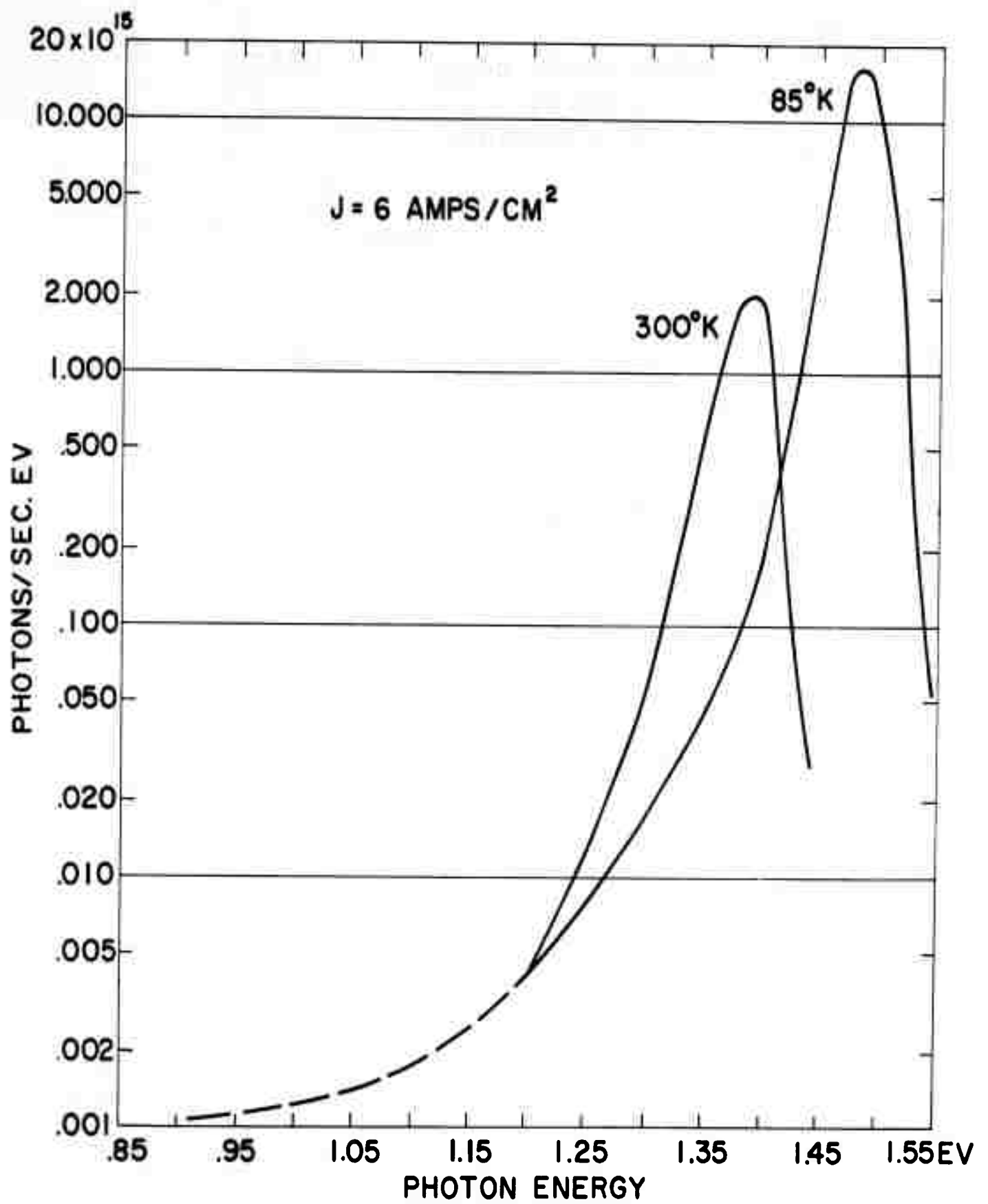


Figure 15. Spectral Distribution With Negligible Low-Energy Radiation

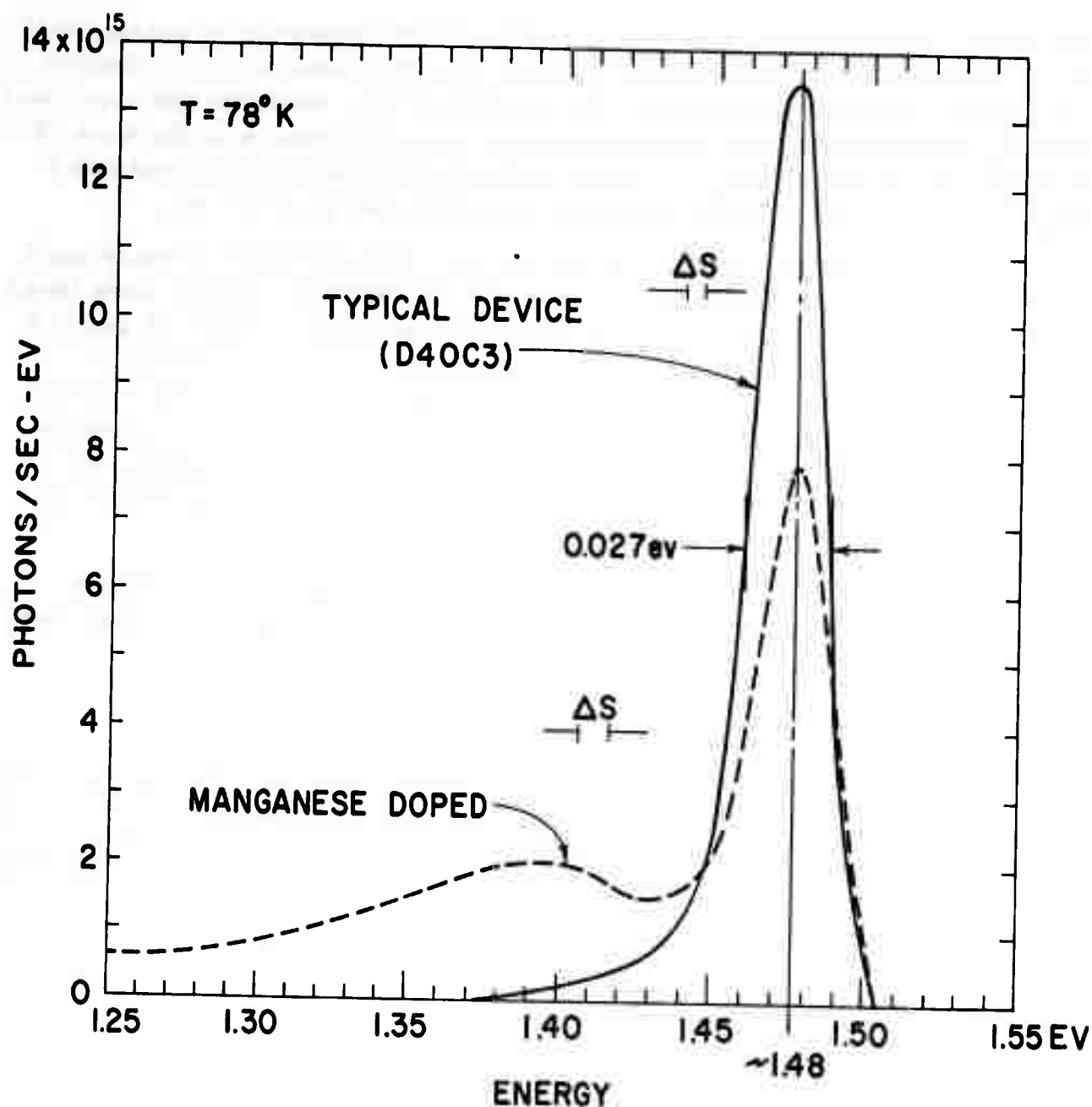


Figure 16. Spectral Distribution  
of Typical and Manganese Compensated Devices

This typical device characteristic refers to zinc diffused units fabricated with N-type starting material of  $10^{17}$  donors/cm<sup>3</sup>. Some units show spectral characteristics such as in Figure 15 where the radiation at low energies is below the detection threshold of the spectrometer.

Infrared sources fabricated on N-type wafers compensated with manganese were compared with typical units. A strong secondary radiation peak was observed at an energy level 0.1 eV removed from the primary emission maximum. This spectral characteristic for a manganese device is compared with an uncompensated device in Figure 16. Manganese compensation does not appear to affect the integrated photon flux appreciably in this case, but does reduce the photon energy and hence the energy conversion



efficiency. The radiation peak introduced by the manganese at an energy level 0.1 ev removed from the primary radiation maximum may be interpreted as due to deep lying energy levels 0.1 ev removed from a bandedge and associated with the manganese dopant. This hypothesis is in agreement with the work of Vieland<sup>6</sup> who deduced from Hall measurements that manganese introduces a single impurity level into GaAs with an ionization energy of 0.1 ev.

Measurements of the spectral characteristics of many units obtained using different fabrication processes and starting crystals show lower energy (long wavelength) spectral peaks at approximately 0.9 to 1.05 and 1.3 ev which are best defined at lower temperatures. The two low-energy peaks of Figure 16 are further illustrated by Figure 17 which is obtained with a diode fabricated in different starting material and different diffusion equipment. The nature of the low-energy radiation peaks is not understood, but must be due either to defect levels or an impurity which has been present in each sample.

The spectral peaks reported in the literature by various investigators for GaAs are summarized in Table II; both injection luminescence and photoluminescence values are included.

Table II. GaAs Spontaneous Emission Peaks

Investigator	Injection		Photo 77°K
	77°K	300°K	
Texas Instruments	1.48(Zn), 1.40(Mn), 1.3, 0.9, 1.05	1.38, 1.3, 0.9, 1.05	
Nasledov et.al. <sup>7</sup>	1.47		
Pankove and Massoulie <sup>8</sup>	1.45(Zn), 1.36, 0.95	1.38, 0.95	
Keyes and Quist <sup>9</sup>	1.44(Zn), 1.26, 0.95	1.33, 0.95	
Nathan <sup>2</sup>			1.51(Te), 1.48(Zn)

Interaction between two or more radiation mechanisms may occur in the GaAs sources. Some devices show saturation effects with increased current for one spectral peak while another spectral peak may show superlinearity (Figure 18).

The primary emission peak closely follows the variation of bandgap with temperature, shifting to higher energy as the temperature is decreased. Table III summarizes the measured values of emission energy, wavelength, and linewidth for zinc-diffused sources made from wafers doped  $10^{17}$  donors/cm<sup>3</sup>.

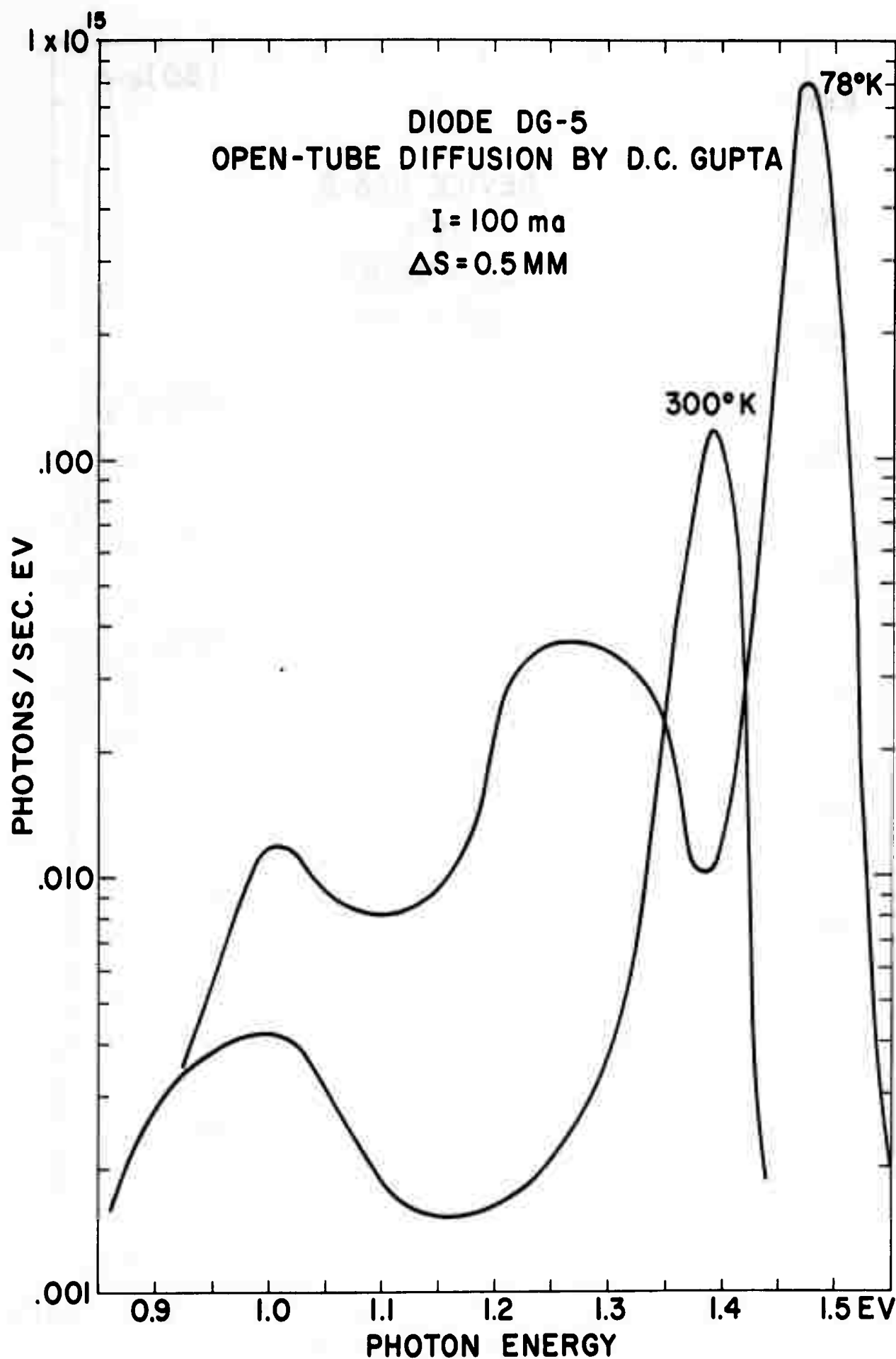


Figure 17. Spectral Distribution With Modified Diffusion Process

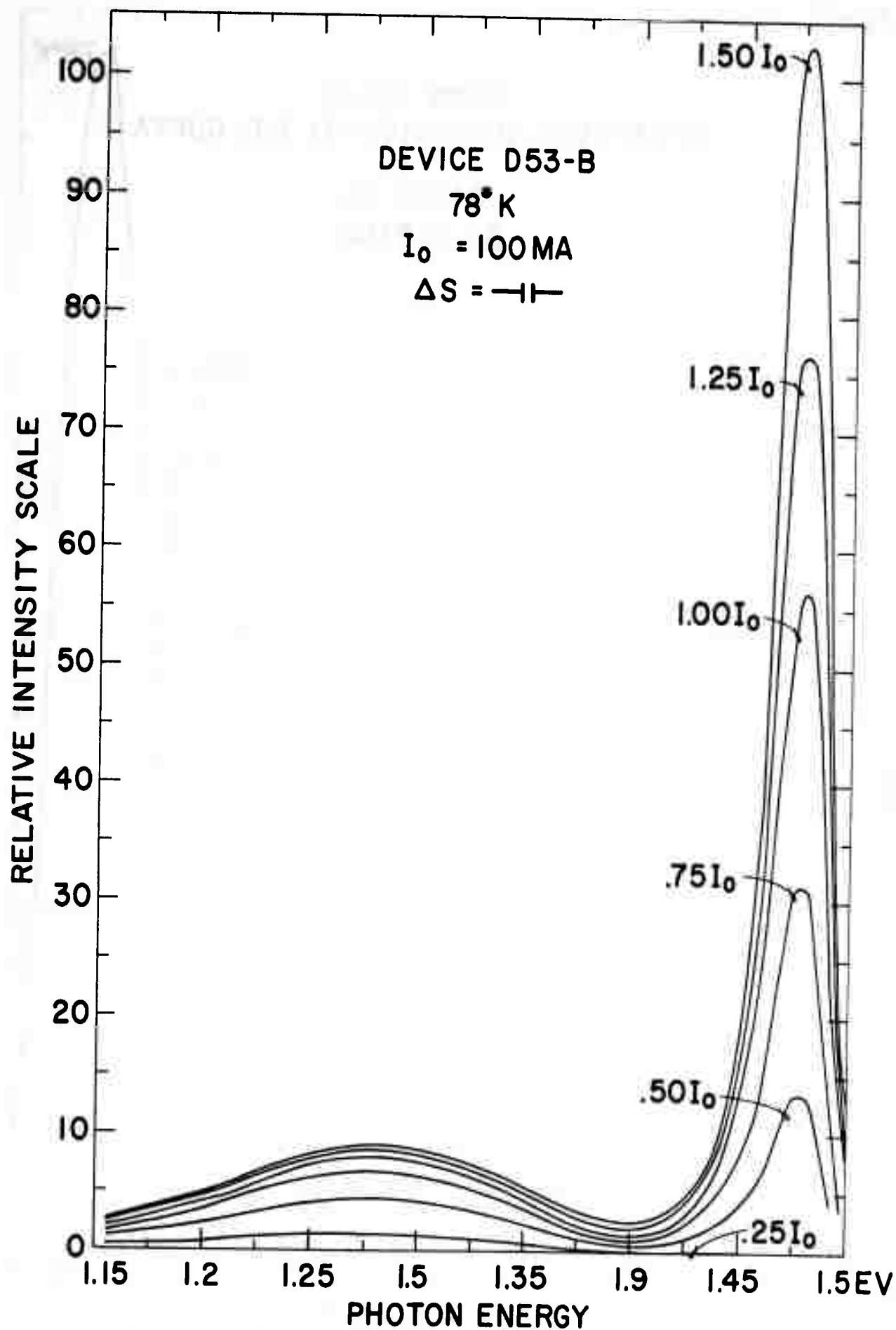


Figure 18. Spectral Distribution Showing Saturation Effects

Table III. Spontaneous Emission Spectral Characteristics

T	$\lambda_p$	$\Delta\lambda$	$E_p$	$\Delta E$
$^{\circ}\text{K}$	Microns	Angstroms	ev	ev
400	0.92	350	1.35	0.050
300	0.90	250	1.38	0.041
200	0.86	200	1.44	0.033
160	0.85		1.46	
100	0.84	150	1.48	0.024

### c. Frequency Response and Modulation

The plot of Figure 3 indicates the infrared radiation is a linear function of the forward current for currents greater than 10 ma. This linear dependence between infrared radiation and current is one of the unique features of the GaAs infrared source and represents the most straightforward technique for modulating the infrared radiation.

The equivalent circuit of a GaAs diode is given in Figure 19. The junction capacitance,  $C_j$ , sometimes called the depletion region capacitance is given by

$$C_j = C' (V + \phi)^{-1/2} \quad (19)$$

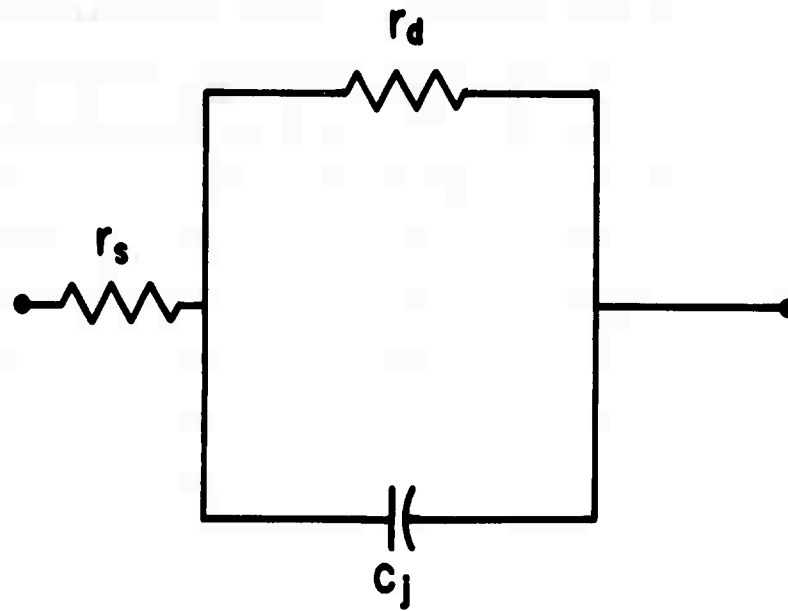
where  $C'$  is a constant depending on doping level and area;  $V$  is the applied bias being negative for forward bias;  $\phi$  is the built-in voltage or contact potential. At zero bias for a  $1.6 \times 10^{-2} \text{ cm}^2$  junction (50 x 50 mil),  $C_j$  will be of the order of 1000 pf; for forward bias, this value may increase to 4000 pf. The diode resistance,  $r_d$ , is given by

$$r_d = \frac{kT}{qI} \quad (20)$$

where  $k$  is Boltzmann's constant,  $T$  is the absolute temperature,  $q$  is the electronic charge, and  $kT/q = 0.026$  volt at  $25^{\circ}\text{C}$ . For a 1.3-amp forward bias  $r_d = 0.02$  ohm.

With constant current drive the series resistance,  $r_s$ , is in series with the high impedance source and the internal cutoff frequency for small signal modulation about the 1.3-amp bias current is

$$f_c = \frac{1}{2\pi r_{dc}} \cong 2\text{kMc} \quad (21)$$



$$r_d = \frac{kT}{qI}$$

$$C_j = C' (V + \phi)^{-\frac{1}{2}}$$

Figure 19. Diode Equivalent Circuit

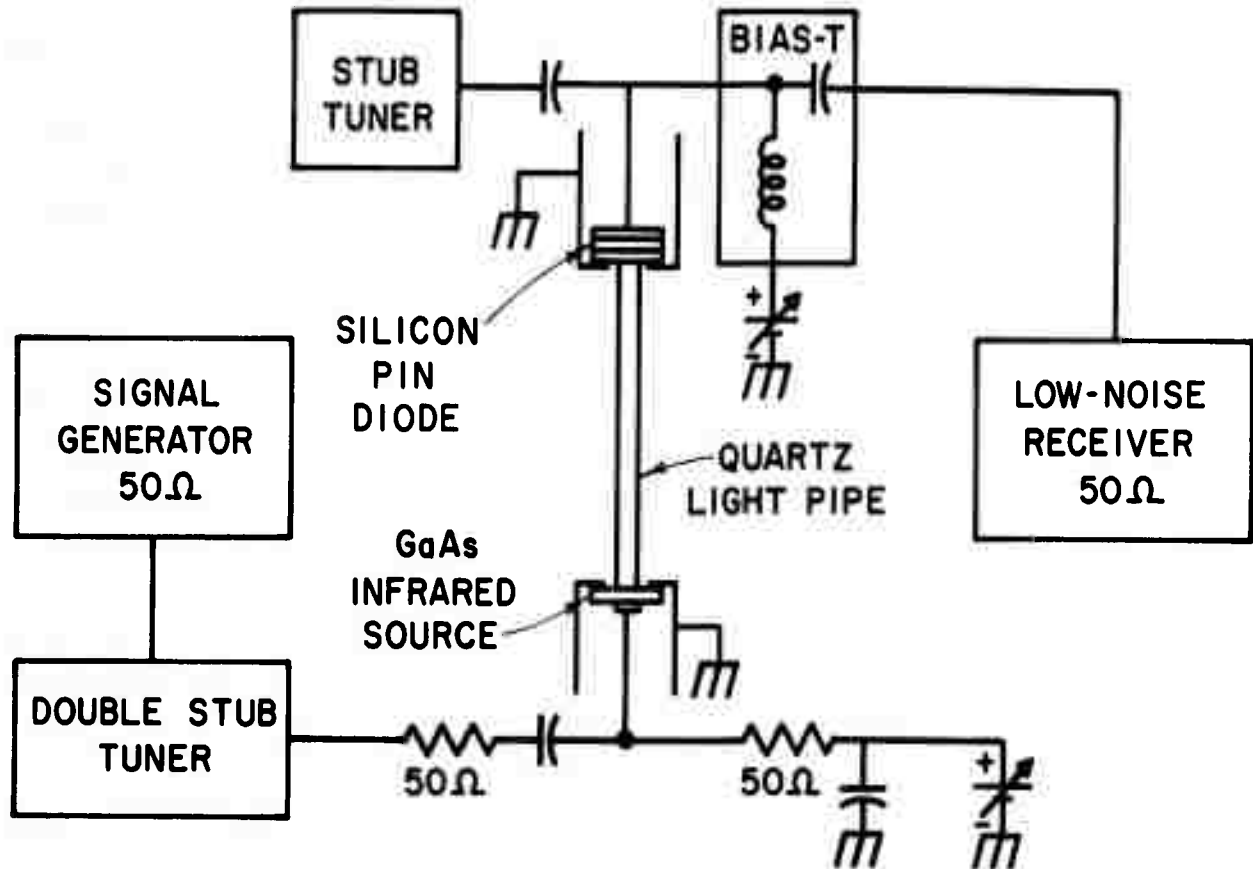


Figure 20. Schematic of Modulation Test Equipment

Since it is the component of current flowing in  $r_d$  which is partially converted to infrared emission, this cutoff frequency is the result of the bypassing effect of the junction capacitance. For pulse operation, the response will not be as fast due to the necessity of charging  $C_j$ .

There is also a frequency limitation imposed by the bulk lifetime in the diode. The lifetime must be short compared to the period of the modulating signal in order for the infrared radiation to follow the diode current.

Microwave modulation capability of the infrared source diodes was successfully demonstrated using the test equipment represented schematically in Figure 20. The 50-ohm signal generator was matched into the 50-ohm current limiting resistor to provide a constant current drive for the infrared source which was forward-biased to 100 ma dc. The P-I-N silicon diode detector was reverse-biased to 125 volts and tuned with the single stub. Signal at the receiver input indicated the presence of optical coupling through the quartz light pipe. This measurement was successfully performed at various frequencies between 500 and 900 mc as limited by the range of the test equipment. No tendency to cut off was noted in this frequency range, and higher modulating frequencies should be possible.

#### d. Spatial Radiation Pattern

The radiation from a flat unit is measured to follow closely that for a black body radiator, i.e., the intensity pattern follows a  $\cos \beta$  variation for a detector at constant distance from the radiator, see Equation (6). A comparison of the measured data with that calculated from the Fresnel equation is shown in Figure 21 and closely approximates a circular pattern. No significant deviation from this radiation pattern has been observed with the flat units; the pattern is unchanged over the temperature range from liquid nitrogen to room temperature.

#### e. Life Test Data

Units for this test were selected at random from production runs of the SNX100. Final test for the SNX100 includes 24-hour operation with 100-ma bias (6 amp/cm<sup>2</sup>) in 25°C ambient (P-N junction temperature approximately 100°C). The tests were as follows:

Test (a)—18 units at 100 ma in 25°C ambient

Test (b)—6 units with no power in 125°C ambient.

The IR output of these units has been measured periodically through the test, which has now completed 3000 hours. The outputs have remained constant within the measuring accuracy, thus indicating no systematic degradation through the 3000-hour period.

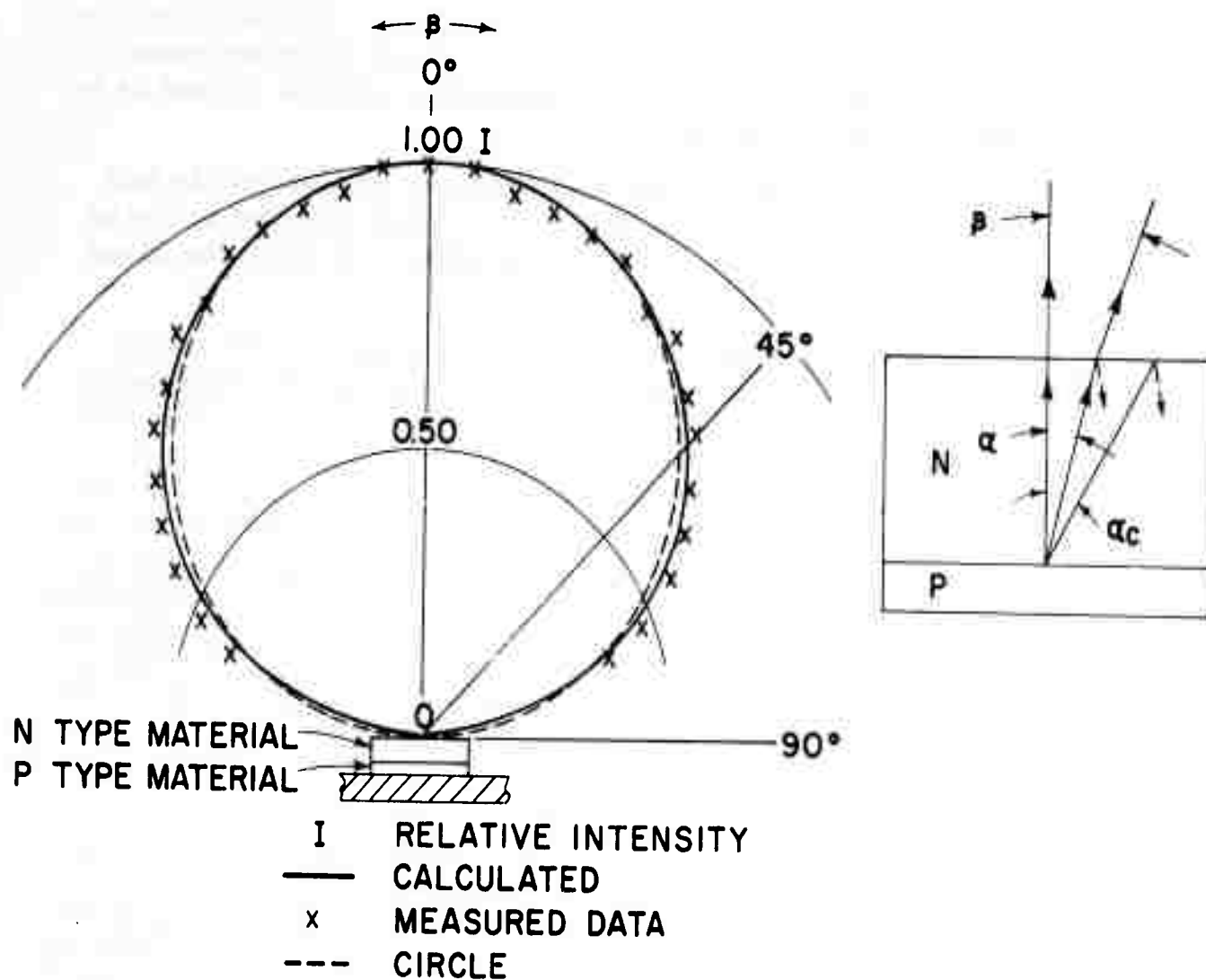


Figure 21. Radiation Intensity Pattern for the Flat Geometry

### C. COHERENT INFRARED EMISSION

#### 1. Introduction

Several authors have recently reported the observation of stimulated (coherent) emission from flat geometry GaAs diode structures.<sup>10,11,12</sup> In the laser mode, the infrared is emitted in the plane of the P-N junction as a result of an injected population inversion. In this mode, radiative recombination by stimulated emission becomes more probable than spontaneous radiative recombination and nonradiative recombination. Thus, a laser mode diode should have a high internal quantum efficiency. Since all the emitted radiation strikes the GaAs-air interface normal to the surface, the transmission efficiency should also be high. A narrowbeam, high quantum efficiency infrared source would be very useful in electro-optical Functional Electronic Blocks. At the present time the laser mode of operation requires high current densities ( $\approx 10,000$  amp/cm<sup>2</sup>); however, it may be possible to overcome this difficulty.

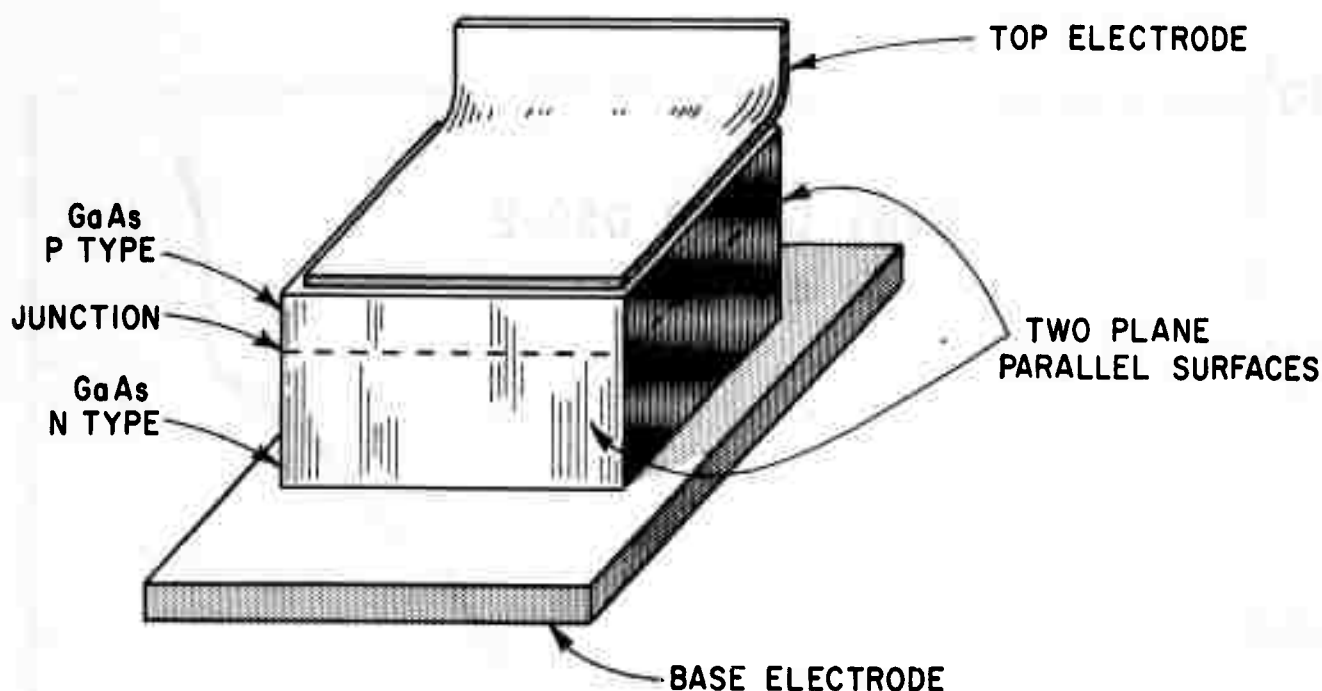


Figure 22. Laser Geometry and Fabrication

## 2. Stimulated Recombination Mechanism

Several workers have proposed that at sufficiently high injection levels one may obtain stimulated photon emission in semiconductor diodes.<sup>13-19</sup> The stimulated emission observed in the GaAs diodes constructed at Texas Instruments occurs at a longer wavelength than the spontaneous emission and appears to be somewhat independent of the spontaneous emission characteristics of the diode, unlike the case for optically pumped laser materials. It has been proposed<sup>20</sup> that the sharp exciton lines observed in semiconductors (including GaAs<sup>21</sup>) may provide the narrow fluorescence line necessary to support lasing.

## 3. Laser Geometry and Fabrication

The structure of the GaAs laser diodes fabricated during this quarter is shown in Figure 22. These devices were fabricated using a standard zinc diffusion into a chemically polished 111 face with the plane-parallel ends formed by cleaving on the 110 plane which is perpendicular to the junction. Some difficulty has been encountered in these devices due to lensing of the chemically polished surface. In order to avoid the lensing, a few laser structures have been fabricated in which all faces were mechanically polished to an optical finish. The Fabry-Perot interferometer is formed by the plane-parallel cleaved ends and the emission is in the plane of the junction perpendicular to interferometer surface.

## 4. Laser Performance

The photon flux measured with a detector in the plane of the junction as a function of pulsed current is shown in Figure 23 at 4.2°K.



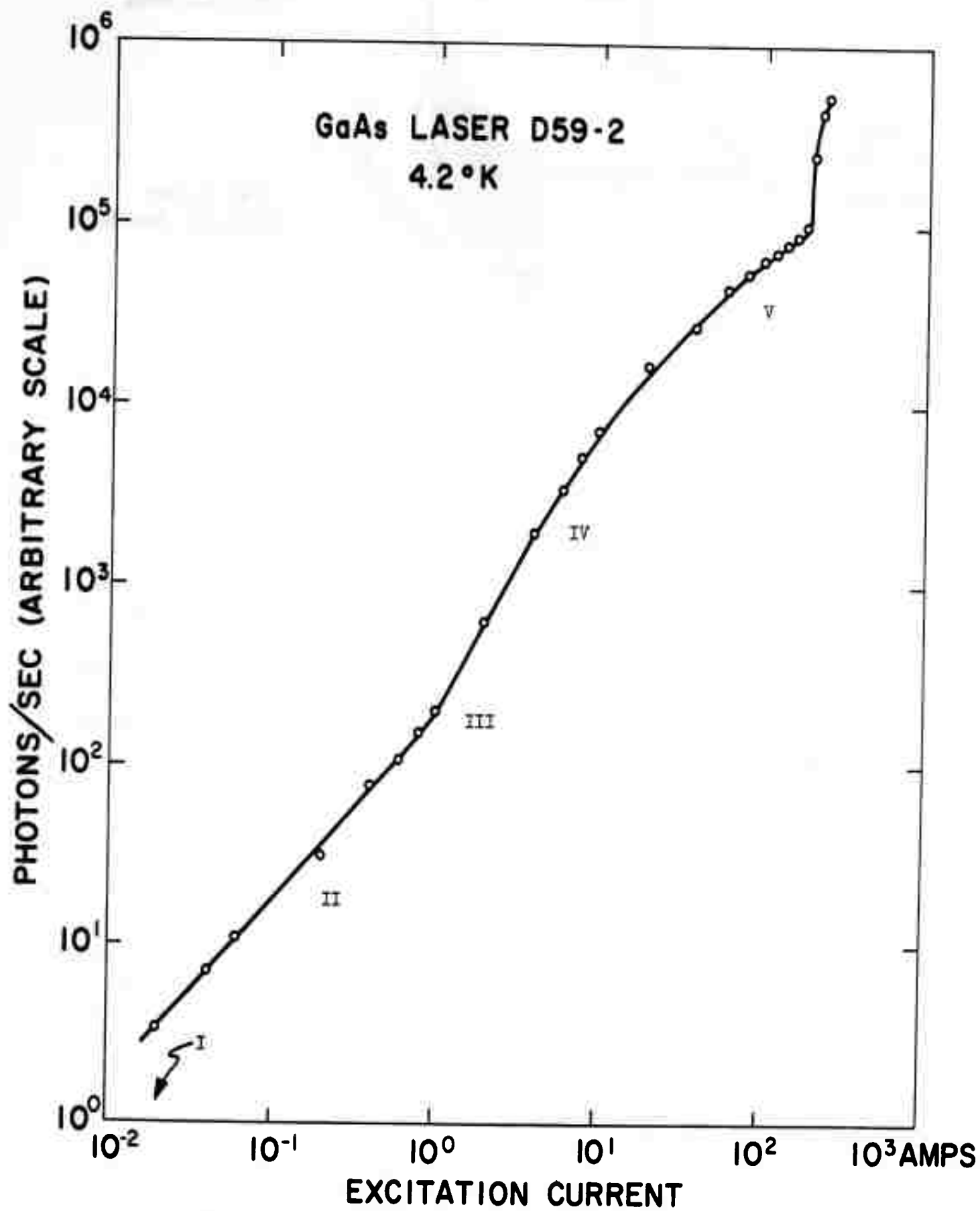


Figure 23. Laser Output Versus Excitation Current

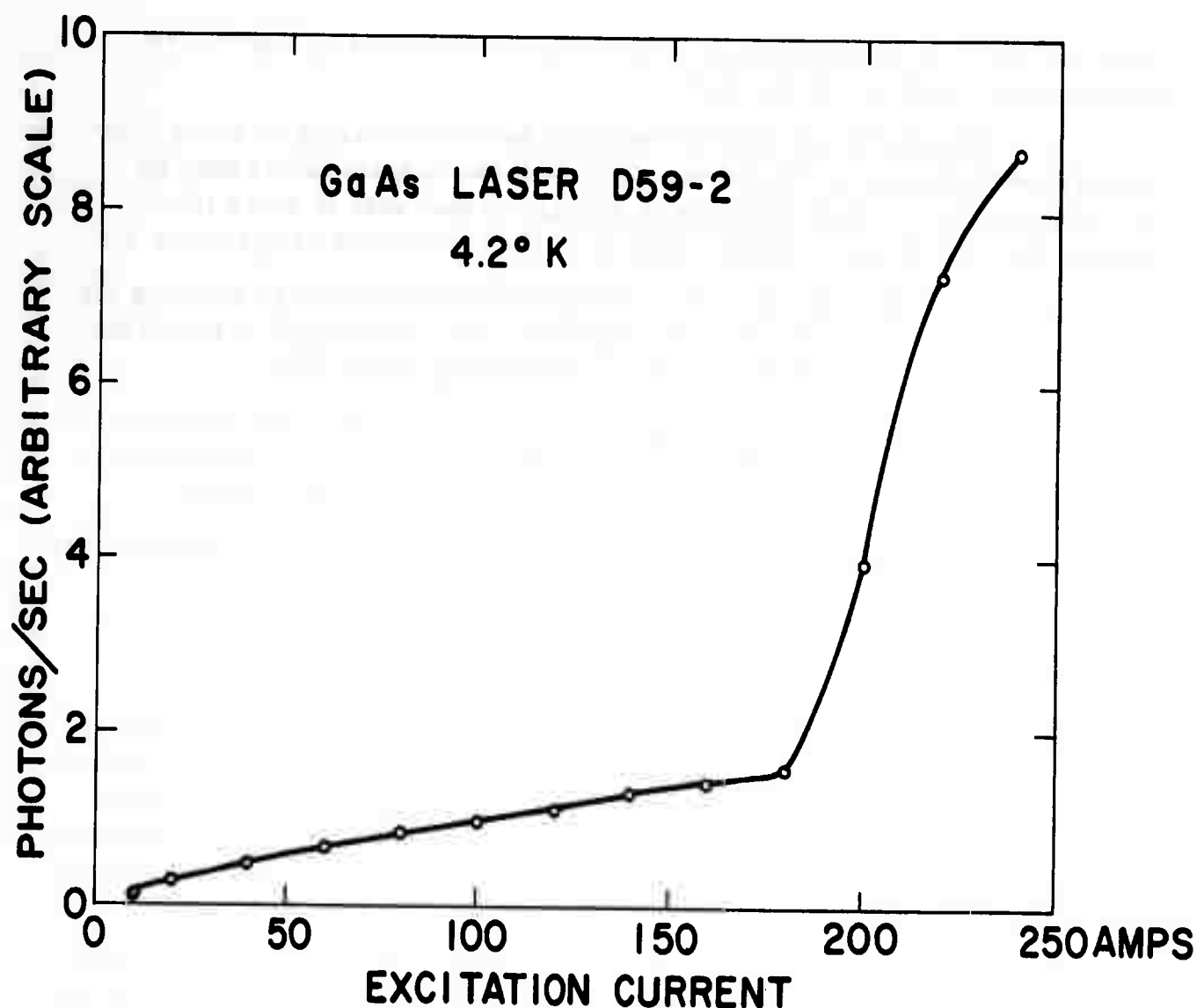


Figure 24. Expanded Scale Laser Output Versus Excitation Current

The various modes of operation of this device are characterized by the slope of the characteristic; five distinct regions are summarized below.

- I Superlinear
- II Linear
- III Superlinear
- IV Linear
- V Superlinear-Lasing.

Laser action as well as the region of highest quantum efficiency, V, occurs at the highest current level, where the emission is accompanied by a narrowing of the emission linewidth—an expanded plot of this region is shown in Figure 24. The superlinearity of Region I is due to the presence of the  $nkT$  perimeter current. Region II is the normal spontaneous emission mode of operation. The presence of Regions III and IV is not completely understood; this characteristic is probably associated with a form of stimulated emission

which is not truly coherent because it is not accompanied by any discrete optical mode selection in the wafer.

The excitation current required to achieve lasing is above 1000 amps/cm<sup>2</sup> in present units and operation at these current levels may be accompanied by a device degradation similar to that seen in GaAs tunnel diodes. Several of the favorable aspects of the laser mode of operation are:

Infrared radiation comes from the wafer edge allowing the entire wafer surface to be covered with a low resistance contact—no debiasing, lower  $I^2R$ .

Infrared radiation is confined to a sheet in the plane of the junction. This results in the minimum detector area for efficient collection of the infrared energy.

Spectral linewidth is much narrower than in the spontaneous emission mode.

#### D. PLANS

The work planned on this task during the next quarter will consist primarily of a continuation of the study of spontaneous and stimulated recombination mechanisms in GaAs. The aim of these studies will be to gain a better understanding of the radiative processes and maximize the quantum efficiency and power efficiency of the three basic device configurations: flat geometry, dome geometry, and laser.

More specifically, the bulk absorption of N- and P-type GaAs and the internal reflectivity of the contacts will be investigated. The results of these measurements will allow a more accurate determination of the internal quantum efficiency of the spontaneous sources. A continuing evaluation of the effect of changes in the various process steps and starting material is planned for both the spontaneous emission source and laser.

## SECTION II

### TASK II—LIGHT MULTIPLEXING

#### A. INTRODUCTION

A multiplex network has been selected as the first application for the GaAs IR source to FEB's. This device is to be a low-level photochopper in which the impedance of a silicon device will be modulated by IR radiation from a GaAs source. However, the task is somewhat broader in scope in that solutions of optical coupling problems for this FEB will be directly applicable to other networks utilizing the IR source.

The first phototransistor tested for this application (prior to the present contract) indicated the need for transistors with higher inverse  $\alpha$ . As a result, new photomasks have been designed and fabricated which should yield transistors with improved characteristics. The transistors will be made by the Networks Technology Facility, which has the latest techniques and equipment for silicon device fabrication.

Emphasis during the first quarter has been primarily aimed at increasing the efficiency of the IR source, and investigating potential methods of optically coupling the source and detectors.

#### B. OPTICAL DESIGN CONSIDERATIONS

##### 1. Transmission Efficiency

Significant improvement in optical coupling between the GaAs source and the phototransistor detector can be achieved by getting more of the generated light out of the GaAs wafer. The transmission efficiency of a flat geometry was evaluated as  $\eta_T = 1.57$  percent; this assumed complete absorption in the P-type layer. If the diffusion experiments on etch-polished surfaces are interpreted as implying considerable reflection from the alloyed P-layer contact, then a typical value for transmission efficiency is  $\eta_T = 3.0$  percent. This may be increased to  $\eta_T = 4.6$  percent by use of an antireflection coating or it may be increased to  $\approx 100$  percent by shaping the N-type GaAs wafer in the form of a hemisphere and using an antireflection coating.

##### 2. Hemispherical Domes

Figure 25 illustrates some of the design criteria associated with a hemispherical geometry. If all the radiation originated at the center of the hemisphere, every ray would intersect the surface on the normal and would be transmitted. An actual device contains a junction of finite size and moreover some applications may require large currents so that it is of interest to determine the maximum ratio of junction radius to hemisphere radius which will still allow essentially all of the radiation to be transmitted.

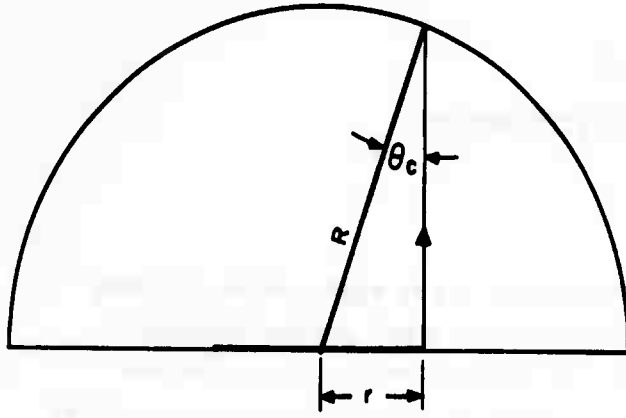


Figure 25. Cross Section of Hemispherical Structure

Referring to Figure 25, it can be shown that essentially all of the radiation is transmitted when the junction radius is such that a ray originating at the edge of the junction and normal to the flat surface of the hemisphere intersects the curved surface of the hemisphere at the critical angle. Since by definition the sine of the critical angle is  $1/n$  where  $n$  is the index of refraction of the material forming the hemisphere, and the transmission is into air, then:

$$\sin \theta_c = \frac{r}{R} = \frac{1}{n} \quad (22)$$

$$r = \frac{R}{n} ,$$

since for gallium arsenide  $n = 3.3$ ,  $r \approx 0.3R$  .

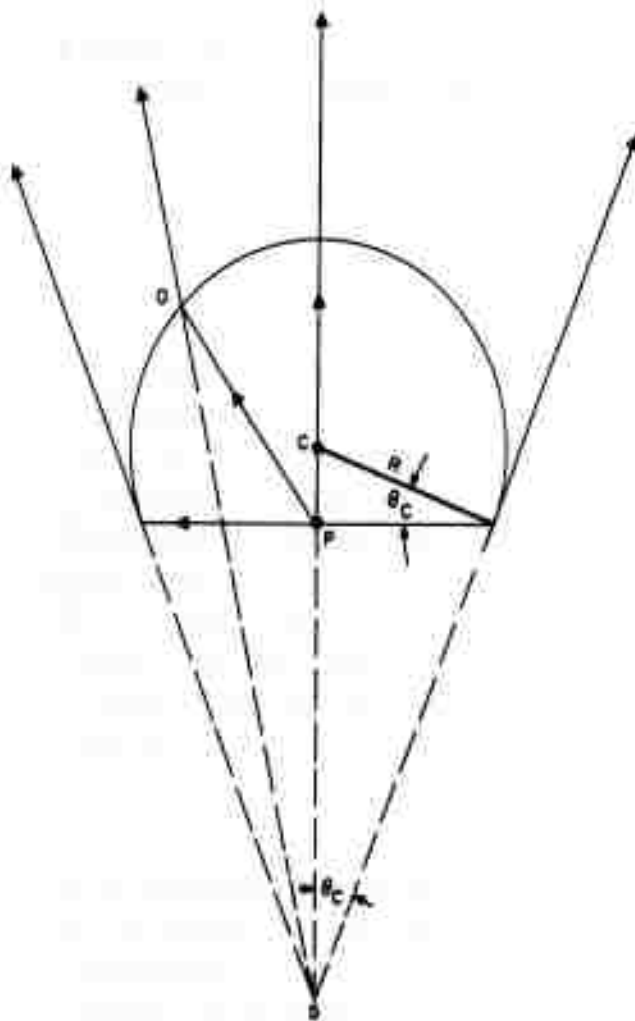


Figure 26. Cross Section of Weierstrass Sphere

Another structure of potential interest is the Weierstrass sphere illustrated in Figure 26. The sphere is constructed such that the distance from the true center of the sphere to the point P (the point from which all radiation is considered to originate) is:

$$CP = R \sin \theta_c , \quad (23)$$

or for gallium arsenide:

$$CP = \frac{R}{3.3} \approx 0.3R. \quad (24)$$

It can be shown that any ray which leaves the surface of the hemisphere appears to have originated at the point S. The distance from the point P to S along the normal to point P is:

$$SP = \frac{R(n^2 - 1)}{n} , \quad (25)$$

where  $R$  is the radius of the sphere and  $n$  is the index of refraction. In addition, all of the radiation is contained in a solid angle  $2\theta_c$  from the apparent point

of origin S. For gallium arsenide  $2\theta_c$  is approximately 35 degrees so that considerable focusing could be obtained from such a geometry by comparison to a true hemisphere.

The light output from a hemispherical device could be expected to increase as much as a factor of 20 compared to a flat device provided absorption remains negligible in the thicker N-type material.

### C. COUPLING MEDIA

For flat geometries, a transparent coating with a refractive index larger than that of air will increase the angle for total internal reflection, and improve the transmission into the coating. For example, the critical angle for total internal reflection can be increased from 17.5 degrees for a gallium arsenide-air interface to nearly 26 degrees by using a coating with a refractive index of 1.43 such as Sylgard.

As a result, the transmission into the coating is more than twice that into air. However, it can be shown that if the surface of the coating is flat, no advantage is gained due to this increase in critical angle. Since the radiation from the coating into air is the radiation which would have been transmitted directly into air from the gallium arsenide, the extra radiation in the coating is internally reflected at the coating-air interface. If the coating is applied in the form of a hemisphere, however, all of the radiation transmitted into the coating will be within the critical angle at the coating-air interface if the radius  $R$  of the hemispherical coating is such that:

$$R = r \cdot n \quad (26)$$

where  $n$  is the index of refraction of the coating and  $r$  is the radius of the plane-radiating surface. The foregoing result is obtained using an analysis identical to that for the hemispherical geometry discussed earlier.

Another perhaps more significant advantage of such a coating is its effect on the reflection coefficient which causes a loss at an interface even for radiation intersecting the interface at normal incidence. The reflection coefficient for normal incidence is defined as:

$$R = \left( \frac{n_2 - n_1}{n_2 + n_1} \right)^2 \quad (27)$$

where  $n_1$  and  $n_2$  are the refractive indices of the two media.

For a gallium arsenide-air interface,  $R$  is 28.6 percent; for a gallium arsenide-Sylgard interface,  $R$  is only 15.6 percent; and for a Sylgard-air interface, only 3.1 percent. Thus, for a flat geometry, assuming negligible absorption in the N-layer and complete absorption in the P-layer, it should be possible to change the total transmission coefficient  $\eta_T$  for gallium arsenide to air from about 1.6 percent to about 4 percent by use of a Sylgard dome as described above.

If we consider a gallium arsenide source and a silicon detector coupled by air, the transmission loss at the two interfaces will be about 50 percent, while for the same source and detector coupled by Sylgard, the loss would be only about 30 percent.

#### D. EXPERIMENTAL RESULTS

As a result of the foregoing considerations, a program was initiated to obtain gallium arsenide-infrared sources with hemispherical geometry. The first units were ground and polished by the Optics Shop of the Apparatus Division, and resulted in "domes" with a nominal radius of 30 mils. The best unit was only about twice as efficient as the best flat devices, the problem being apparently that the domes were sectors of hemispheres rather than true hemispheres. The capability for grinding and polishing such domes has since been developed in the Molecular Engineering Device Laboratory and devices have been obtained which are approximately seven times better than the best flat units. While this is a substantial improvement, it is still only one-third the expected output of a dome unit. If this factor of one-third is due to absorption in the N-type material, then the absorption coefficient is approximately equal to the inverse of the radius of the hemisphere.

$$\alpha = \frac{1}{30 \text{ mil}} = 13 \text{ cm}^{-1} . \quad (28)$$

In order to proceed with device design a more accurate value of the absorption coefficient is needed.

Some effort during the quarter was spent in consideration of dielectric coatings to improve the transmission efficiency of IR sources. One coating actually tested was Dow Corning Sylgard silicone resin. This resin is transparent, flexible, has good thermal stability, and an index of refraction of 1.43.

The coating was applied to flat units, and although perfect hemispherical coatings were not achieved, the efficiency increased about 50 percent due to the enhanced transmission.

#### E. PLANS

The new phototransistor structures will be evaluated when they become available, using the best light sources available.

Considerable effort will be directed at obtaining more perfect hemispherical devices. Emphasis will be on obtaining smaller diameters. Design of an optimum structure depends on a knowledge of the effective absorption coefficients in N- and P-type gallium arsenide. For this reason, experiments will be designed and performed to obtain the necessary data.

The radiation patterns of the hemispherical devices must be known in order to design the most effective optical coupling methods. A continuing study will be made of methods and materials for improved light coupling.

### SECTION III

#### TASK III—ACOUSTIC AMPLIFICATION

##### A. INTRODUCTION

Task III is an exploratory investigation of the ultrasonic amplification effect in piezoelectric semiconductors. The material chosen for the initial study was cadmium sulfide (CdS). This report includes a description of the test facility, fabrication technique, and the results of experiments on the CdS amplifiers.

##### B. TEST FACILITY

A block diagram of the equipment assembled to test ultrasonic amplifier samples is shown in Figure 27.

The input transducer is driven by a pulsed rf signal with a carrier frequency in the 10-45 mc frequency range. The rf pulse equipment has a rise

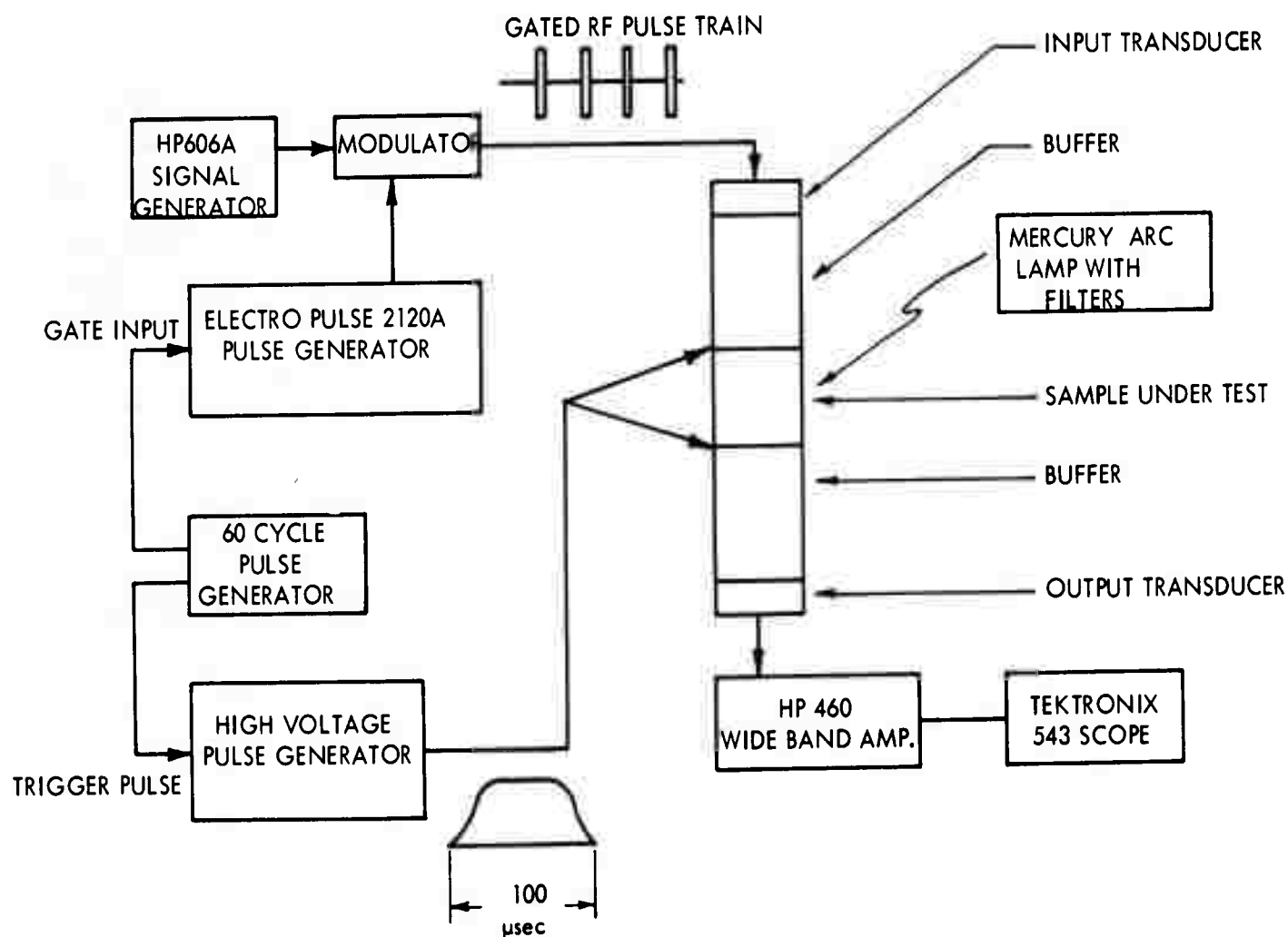
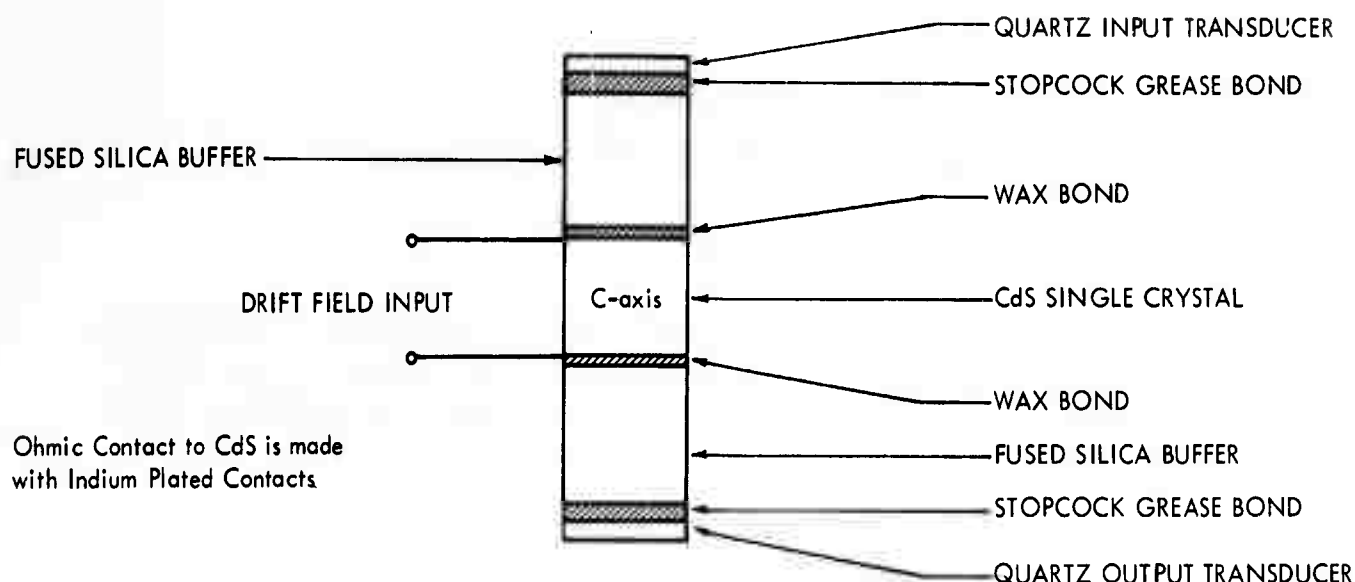


Figure 27. Block Diagram of Test Facility





DIMENSIONS		
Part	Diameter	Length
Transducers	0.25"	-
Buffers	0.25"	1.0"
CdS	0.25"	0.4"

Figure 28. Ultrasonic Amplifier

time of approximately  $0.1 \mu\text{sec}$  and can supply 80 volts (peak-to-peak) across a 200-ohm load. The transmitted rf pulse is detected at the output with two cascaded Hewlett-Packard wideband amplifiers and a Tektronix 543 oscilloscope.

The high voltage pulse for the ultrasonic amplifier drift field is obtained from a charged delay line pulser. The pulse generator is capable of delivering  $100 \mu\text{sec}$ , 200-3300 volt pulses to a 1000-ohm load. The repetition rate of the pulser is 60 pulses per second.

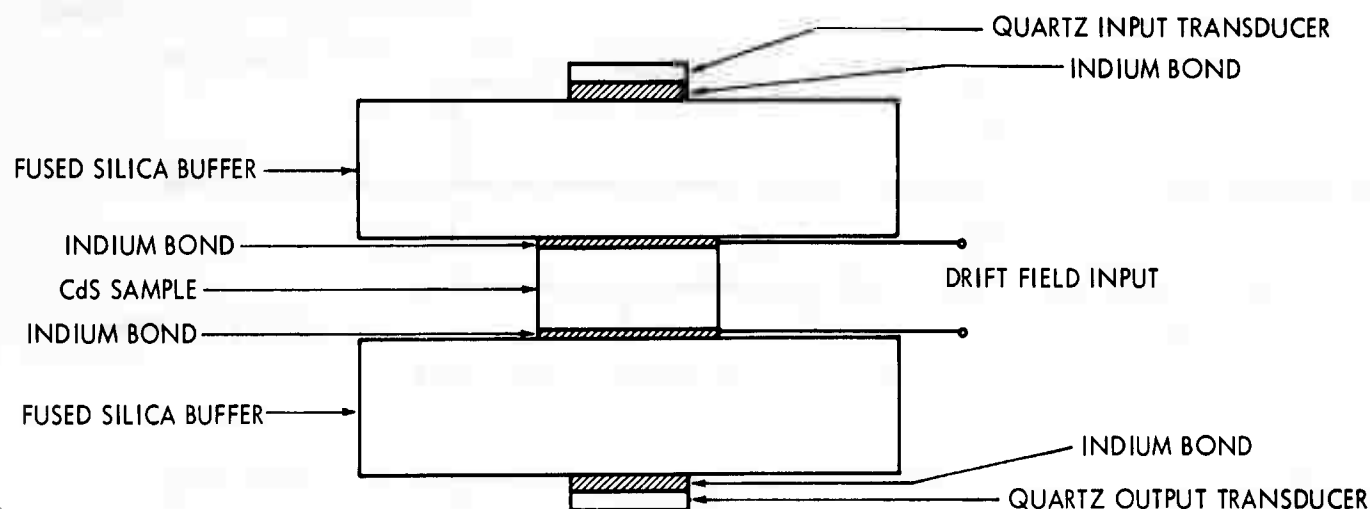
The system is synchronized with line frequency by gating the Electro Pulse 2120A pulse generator and triggering the high voltage pulse generator with the same trigger pulse. Pulses of ultrasonic energy are transmitted through the CdS in synchronism with the drift field pulse. The scope is also triggered from the electro pulse.

The resistivity of the photoconductive CdS is controlled by illuminating the crystal with light of wavelengths of greater than 0.58 micron.

### C. FABRICATION OF ULTRASONIC AMPLIFIER

#### 1. Geometrical Design

The initial configuration used in the ultrasonic amplifier experiments is shown in Figure 28. The assembly consists of quartz transducers, fused silica buffer rods and a CdS crystal all with a diameter of 0.25 inch arranged in the cylindrical form shown in Figure 28. This geometrical



Quartz Transducers are 0.25" in diameter  
 CdS Sample is 0.3" square and 0.2" thick  
 Fused Silica Buffers are 1.25" in diameter and 0.375" thick

Figure 29. Ultrasonic Amplifier

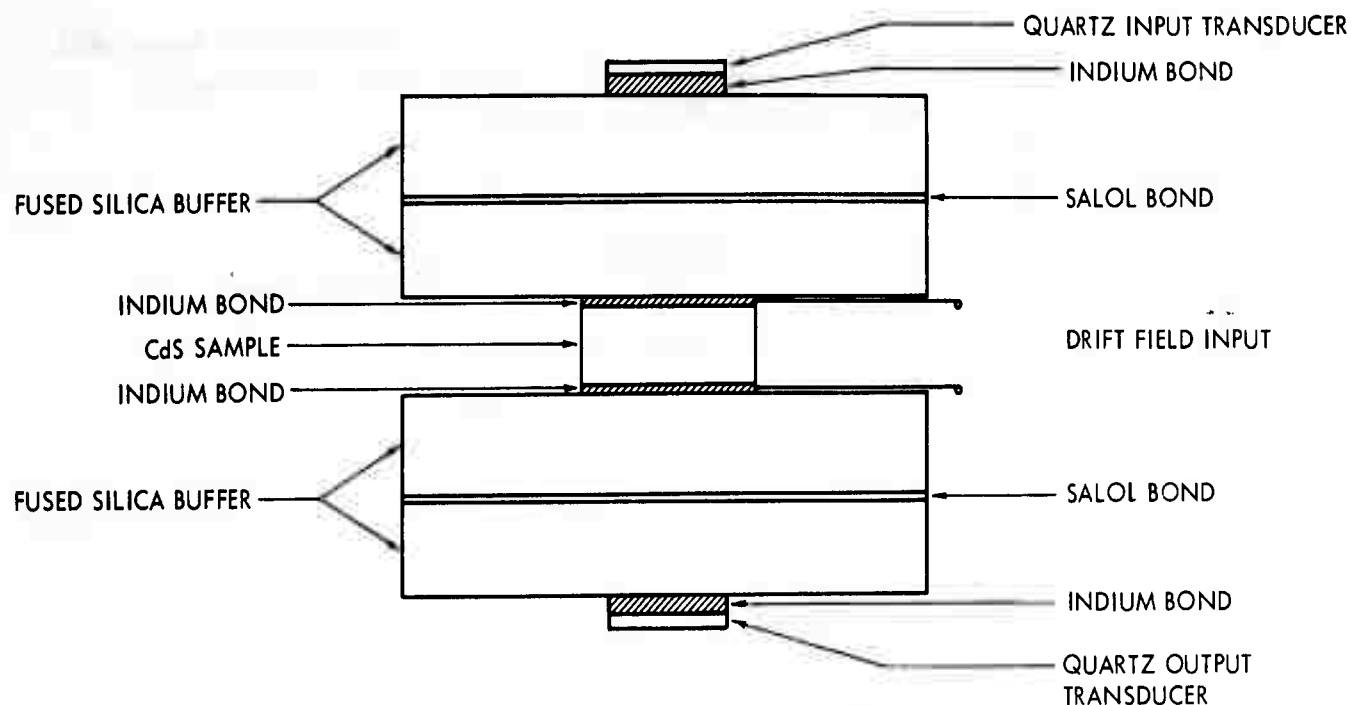
configuration resulted in many spurious reflections caused by the coupling of the ultrasonic waves to the sides of the cylindrical structure.

A new structure was designed which would eliminate edge reflections and allow the propagation of plane waves through the CdS. This structure is shown in Figure 29. The fused silica buffer plates have a thickness which allows the CdS sample to lie within the plane wave region of the quartz transducers. The CdS samples and fused silica buffer plates were made with lateral dimensions as large as practical to prevent coupling of the ultrasonic wave to the edges. The output waveform obtained from this configuration (Figure 29) had reflections from the quartz-CdS interfaces; however, these reflections were predictable and not as undesirable as those in the previous cylindrical arrangements.

Figure 30 shows a modification of the ultrasonic amplifier assembly shown in Figure 29. Here, the quartz transducers are bonded to an auxiliary buffer plate. This eliminates bonding the transducers to the buffer plate for each CdS sample tested and, therefore, allows a series of CdS samples to be tested in a shorter time.

## 2. Sample Preparation

The crystallographic orientation of single crystal boules of CdS is determined by X-ray techniques. The boules are then sawed into single-crystal pieces of the required dimensions and lapped and polished to obtain plane-parallel polished faces perpendicular to the thickness direction of the crystal. Maximum deviation allowed from the nominal thickness dimension is less than 0.1 mil. Sides of the samples are then lapped and polished to nominal dimensions. The sides of the crystals may be etched to obtain diffused light in the CdS sample, if desired.



Quartz Transducers are 0.25" in Diameter  
 CdS Sample is 0.3" Square and 0.2" Thick  
 Fused Silica Buffers are 1.25" in Diameter and 0.375" Thick

Figure 30. Ultrasonic Amplifier

### 3. Bonds and Contacts

#### a. Nonconducting Bonds

Thermoplastic wax, stopcock grease and salol (phenyl salicylate) have been used for making acoustic bonds between the fused silica buffer plates (Figure 30) where no electrical contact is required. For experimental purposes, the most reliable bonds have been made with salol. The melting point of this compound is 43°C making possible the wringing of salol bonds in a liquid state. The Salol bonds are formed by raising the temperature of the buffer plates above the melting point of salol (43°C), wringing one buffer plate onto the other, and then allowing the salol to freeze. Acceptable bonds may be made with thermoplastic wax or stopcock grease. However, these materials are inconvenient to work. The thermoplastic wax must be worked at temperatures above 100°C; the stopcock grease forms a nonrigid bond.

#### b. Conducting Bonds

Indium was chosen for bonding CdS to fused silica because it makes reproducible ohmic contacts to CdS.<sup>22,23,24,25</sup> Fortunately, indium is also a reasonably good acoustic match to both fused silica and CdS as indicated by the data in Table IV.

Table IV. Comparison of Acoustic Impedance  
of CdS, Indium and Fused Silica

Material	Ultrasonic Wave	Acoustic Impedance
CdS	Ext (C-axis)	$20.7 \times 10^6 \text{ Kg}/(\text{M}^2 - \text{sec})$
Fused silica	Ext	$13.6 \times 10^6 \text{ Kg}/(\text{M}^2 - \text{sec})$
Indium	Ext	$8.9 \times 10^6 \text{ Kg}/(\text{M}^2 - \text{sec})$
CdS	Shear (A-axis)	$9.65 \times 10^6 \text{ Kg}/(\text{M}^2 - \text{sec})$
Fused silica	Shear	$8.29 \times 10^6 \text{ Kg}/(\text{M}^2 - \text{sec})$
Indium	Shear	$5.2 \times 10^6 \text{ Kg}/(\text{M}^2 - \text{sec})$

Indium was also used in the ultrasonic amplifier assembly to bond the quartz transducers to the fused silica buffers. The indium bonds are formed by evaporating or electroplating indium on the surfaces to be bonded. A thin foil of indium (1-3 mils) is placed between the faces, and the assembly is placed under heat (120°C) and pressure (approximately 1200 psi) for approximately 24 hours.

#### c. Indium Alloy Bonds

Preliminary investigations have shown that alloys of indium with tin, lead or gold can be used to provide a better acoustic impedance match between CdS, fused silica, and quartz. The improved impedance match would reduce reflections and would be important if delay line applications of the ultrasonic amplifier assembly were being studied. Reduction of interface reflections to a minimum is not significant enough in observing the ultrasonic amplification effect to justify the development of acoustic bonds of adjustable characteristic impedance.

### D. TEST RESULTS OBTAINED FROM ULTRASONIC AMPLIFIER SAMPLES

#### 1. Samples of Cylindrical Geometry

The first group (4 samples) of single crystal CdS received from Harshaw Chemical Company was prefabricated in a cylindrical form. Two of these samples were of resistivity too low to be useful for ultrasonic amplifier experiments in the 10-40-mc range. The other samples were fabricated as shown in Figure 28 to study the propagation of extensional waves along the C-axis. Measured interaction between attenuation of the extensional waves, crystal resistivity (as controlled by light intensity) and drift field is shown in Figure 31. Failure to observe net gains in these samples may be attributed to either low electron mobility (which would require a higher drift field) or trapping levels which would reduce conductivity modulation by the ultrasonic wave. The many reflections observed in the output waveform of this configuration

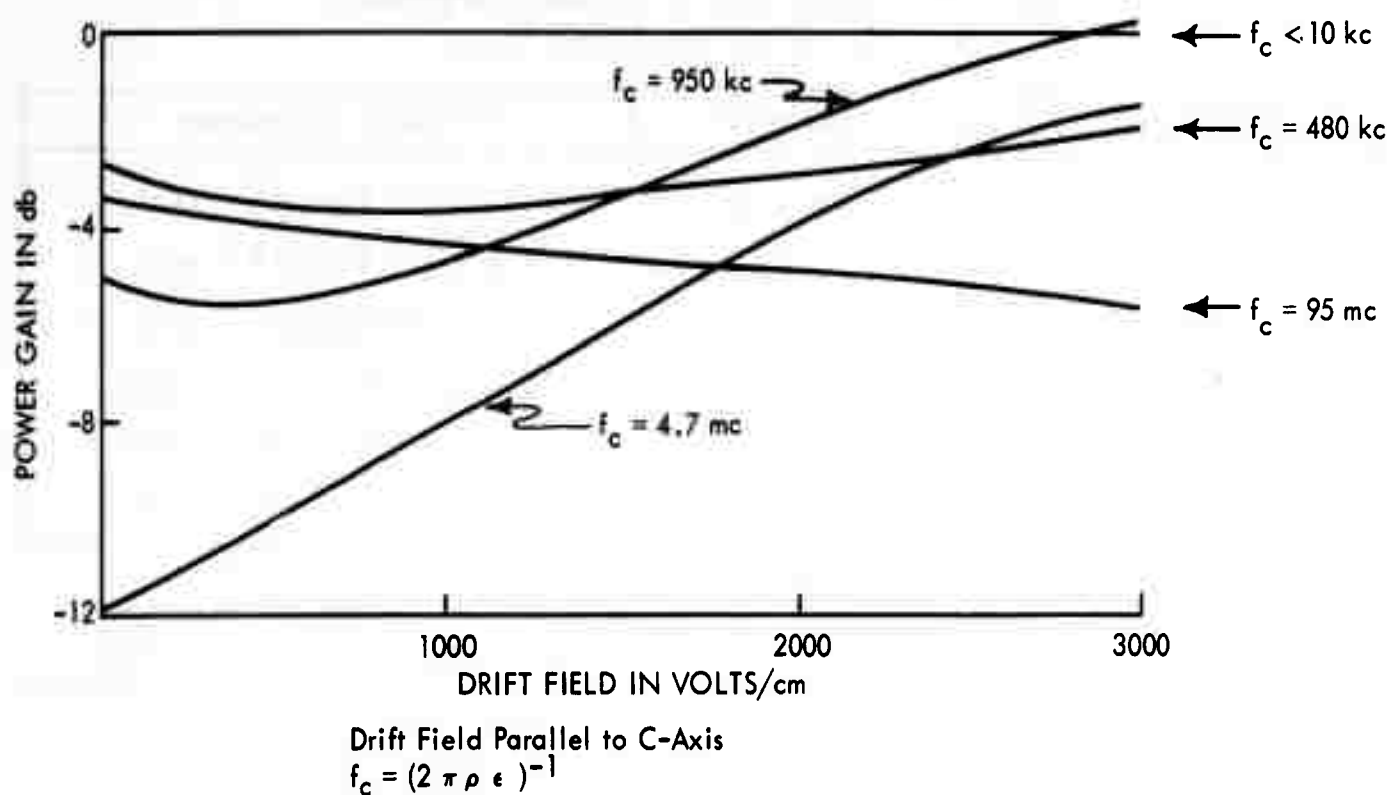


Figure 31. Observed Output for Propagation of 10-MC Extensional Waves Along C-Axis of CdS Versus Drift Field

indicated that changes in geometry and bonding technique were necessary. These samples were destroyed by electrical arcing through the bulk of the crystal before complete data could be obtained.

## 2. Samples With Improved Geometry

### a. Initial Tests

A second group of CdS crystals received from Harshaw had larger lateral dimensions to minimize reflections of the ultrasonic wave from the edges of the crystals. Half of these samples were oriented to allow the study of the propagation of extensional waves along the c-axis. The other half were oriented to allow the study of the propagation of shear waves perpendicular to the c-axis. Approximately half of the crystals in both groups (shear and extensional) were again of a resistivity too low to be useful for ultrasonic amplification experiments in the 10-40 mc range.

Ultrasonic amplifier assemblies were fabricated from the remaining crystals. These assemblies were constructed with indium bonds and large fused silica buffer plates as shown in Figure 29. The resistivity of the crystals used in the ultrasonic amplifier assemblies could not be reduced to the proper range of values with the available light. Thus, very little interaction was observed between ultrasonic attenuation, crystal resistivity, and drift field.

### b. Heat Treatment of Samples

A study was initiated to determine the feasibility of modifying the bulk resistivity and photoconductive properties of the CdS samples by heat treatment. Previous workers have shown that the resistivity of CdS can be increased by heat treatment in a sulfur atmosphere and decreased by heat treatment in air or vacuum.<sup>26, 27, 28, 29, 30</sup>

Results of heat treatment of crystals Nos. 3 and 4 in air, vacuum, and sulfur respectively, are shown in Table V. The data given in Table V shows that the resistance of the CdS crystals has been increased or decreased as predicted. The change in the resistivity was probably not uniform as indicated by the measurements of the ultrasonic attenuation of extensional waves propagated along the C-axis of the samples as a function of crystal resistance and applied drift field. Results of the ultrasonic amplification experiments are given below:

Table V. Heat Treatment of CdS Crystals

Crystal Number	Crystal Resistance in Ohms				Heat Treatment
	Before Heat Treatment		After Heat Treatment		
	Dark	Illuminated By Unfiltered 100w Mercury Arc Lamp	Dark	Illuminated By Unfiltered 100w Mercury Arc Lamp	
3	500	100	$5 \times 10^5$	500	Heated in air for 3 hours at 700°C
6	$5 \times 10^9$	$7 \times 10^4$	$3 \times 10^4$	$5 \times 10^3$	Heated at 20μ pressure for 1/2 hour at 700°C
4	$5 \times 10^3$	-	$5 \times 10^9$	$1 \times 10^5$	Heated in S <sub>2</sub> at 700°C for 32 hours
4	$5 \times 10^9$	$1 \times 10^5$	$> 5 \times 10^9$	$1 \times 10^5$	Reheated in S <sub>2</sub> at 700°C for 100 hours

Crystal 6 treated in vacuum to reduce its dark resistivity showed practically no interaction between acoustic attenuation and resistivity. Application of a field on the order of 1000 volts/cm caused arcing through the crystal which destroyed it.

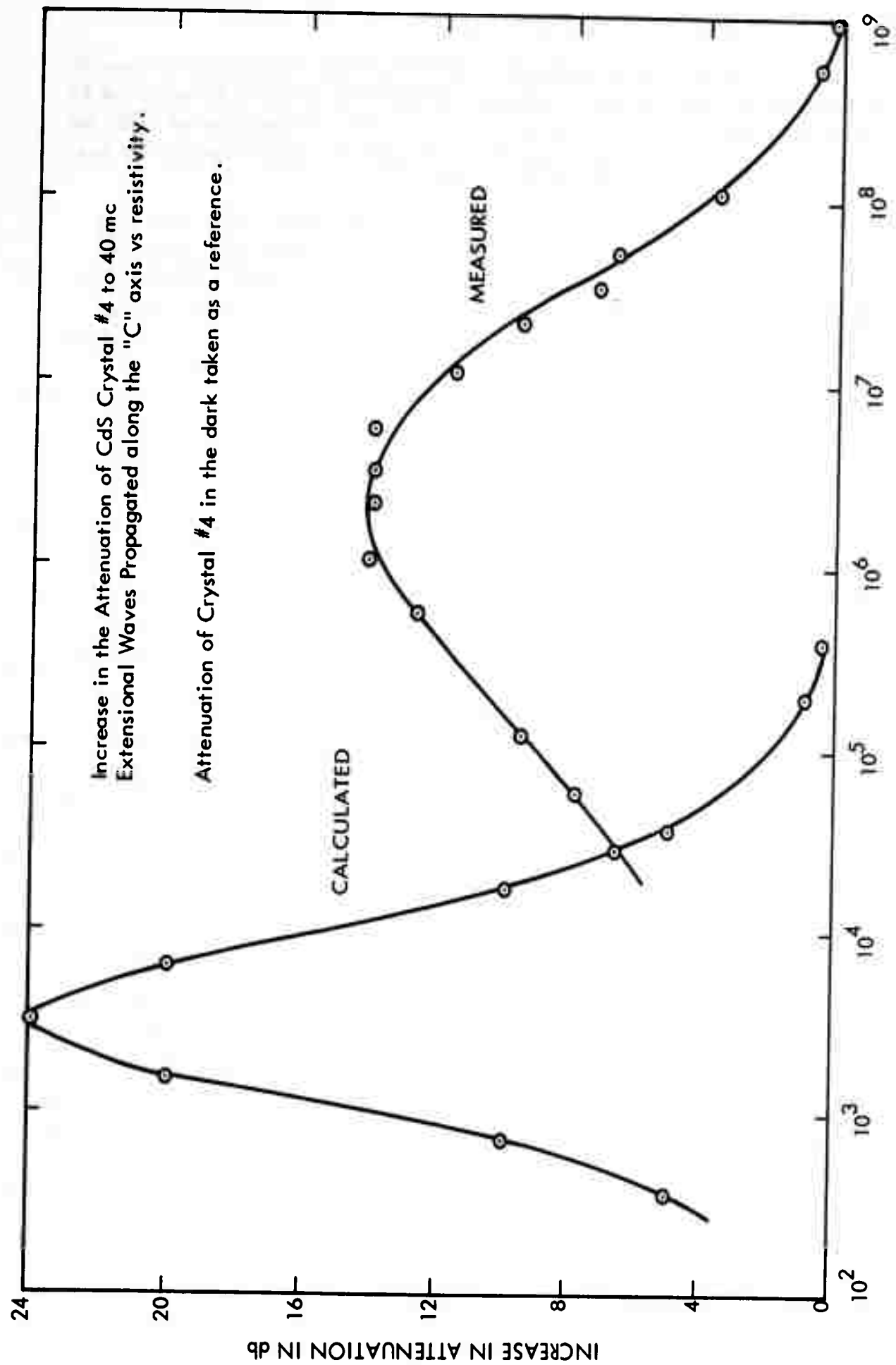


Figure 32. Increase in the Attenuation of CdS Crystal No. 4 to 40 MC Extensional Waves Propagated Along the C-Axis Versus Resistivity

Crystal 3 which had been heat treated in air to increase its dark resistivity did not show an interaction between acoustic attenuation and light intensity. Application of a field on the order of 6000 v/cm returned the crystal to a low resistivity state ( $\rho \cong 250$  ohm-cm) independent of light intensity. This indicates that the resistivity of the crystal was increased only near the surface rather than uniformly through the bulk.

Crystal 4 which had been heat treated in sulfur to increase its dark resistivity showed a small interaction between acoustic attenuation, light intensity and drift field. The resistivity of the crystal remained unchanged throughout the application of fields on the order of 6000 v/cm indicating a more permanent change of crystal properties than that produced by heat treatment in air or vacuum. The magnitude of the attenuation noted indicated again that only a small portion of the crystal was modified to be high resistivity. This crystal was reheated in a sulfur atmosphere at 700°C for 100 hours in an attempt to increase the homogeneity of the crystal. Figure 32 shows the observed change in attenuation of 40-mc extensional waves as a function of crystal resistivity after the additional heat treatment. Maximum attenuation occurs at a resistivity which would be three orders of magnitude too high if the crystal were homogeneous. This indicates that the sulfur treatment has caused a high-resistivity shell to surround the crystal leaving only the center in the proper resistance range to be active to 40-mc waves. The failure to observe interaction between acoustic attenuation and drift field could also be explained by this high resistivity shell.

#### E. CONCLUSION AND RECOMMENDATIONS

The technology necessary for fabricating ultrasonic amplifier assemblies has been acquired during this first reporting period. This has included techniques for bonding the CdS single crystals and the quartz transducers to fused silica buffer plates with indium. Indium was chosen as the bonding material because it makes ohmic contact to CdS and is a reasonable match for the acoustic impedance of quartz, CdS, and fused silica.

The CdS material received to date has been of widely dispersed electrical characteristics as indicated by the large range in crystal resistivity. Only one crystal of the 12 received showed any interaction between ultrasonic attenuation, crystal resistivity and drift field. The resistivity of the other crystals was either too high or too low, making them inactive in the 10- to 40-mc frequency range.

Preliminary heat treatment experiments aimed at modifying the bulk properties of the CdS samples were only partially successful. The resistance of high-resistivity crystals was decreased by heating the crystal in air or vacuum. Heat treatment of low-resistivity crystals in a sulfur atmosphere caused an increase in the resistance of the crystal. However, the bulk properties of only one crystal was changed sufficiently to allow a measurement of the change in ultrasonic attenuation as a function of crystal resistance. The peak attenuation of this sample occurred at a crystal resistance three orders



of magnitude too high for a homogeneous crystal. This indicated that the resistivity of the crystal was not constant throughout the bulk of the crystal.

The modification of bulk crystal properties by simple heat treatment appears impractical at present. Single crystal CdS obtained from a different source may have more desirable bulk properties making elaborate heat treatments unnecessary. Single crystal boules of CdS have been obtained from the Eagle Picher Co. Ultrasonic amplifier assemblies will be fabricated from this material during the next quarter.

## SECTION IV

### TASK IV—THERMAL OSCILLATOR

#### A. OBJECTIVES

Investigation of thermal effects as they apply to semiconductor networks was started during this report period. A literature search of recent articles on the theory of both thermal conduction and thermoelectricity was initiated since both phenomena may be useful for realizing desired network functions.

The specific defined task in this area of investigation is the thermal low-frequency oscillator in semiconductor network form. The frequency determining element of this oscillator will use heat transport (thermal conduction) in silicon for realizing phase shift. This task will include mathematical calculation and corresponding experimental evaluation of the thermal characteristics of various geometric shapes. Most of the information gained can also be applied to the design of filter networks. The remainder of the oscillator will consist of a more or less conventional amplifier to offset the losses of the thermal phase shifting network. Since very little is known about an oscillator of this type, measurements will be made on the complete oscillator to determine the actual performance limits.

#### B. ANALYSIS

The concept of a thermal oscillator in semiconductor network form was essentially due to investigations of observed instabilities of the "temperature stabilized substrate." This circuit function was described in Section IV-C, Report No. 02-62-4, of Contract AF33(616)-8339. A somewhat different description with emphasis on the conditions necessary for oscillation will be given here.

Referring to Figure 33 when  $V_{CC}$  is applied, the voltage at point A determined by the resistor network  $R_1$  and  $R_2$  is less than the  $V_{BE}$  of  $Q_1$  required for conduction, i.e.,  $I_1 = 0$ . Resistor  $R_3$  is much larger than the input impedance of  $Q_2$  and determines the current  $I_3$  ( $I_3$  is practically constant). Since  $I_1$  is zero,  $I_3$  is equal to  $I_4$  and is the base current of  $Q_2$ . The collector current  $I_2$  is approximately  $h_{FE}Q_2I_4$ . The product of the applied voltage  $V_{CC}$  and the current  $I_2$  is the power dissipated as heat in the collector region of  $Q_2$ . This raises the temperature in this region, and a temperature gradient is established causing a heat flow outward from  $Q_2$ . All the components are fabricated on a single substrate; therefore, the temperature at the base-emitter region of  $Q_1$  will be increased, and the  $V_{BE}$  required for conduction is reduced. At some temperature the current  $I_1$  is no longer zero, i.e.,  $Q_1$  starts to conduct. Since  $I_3$  is practically constant, this reduces the base current to  $Q_2$  and consequently the collector current  $I_2$ . Reducing  $I_2$  reduces the heating effect, until an equilibrium point is eventually reached where there is just enough heat supplied to maintain the  $Q_1$  base-emitter

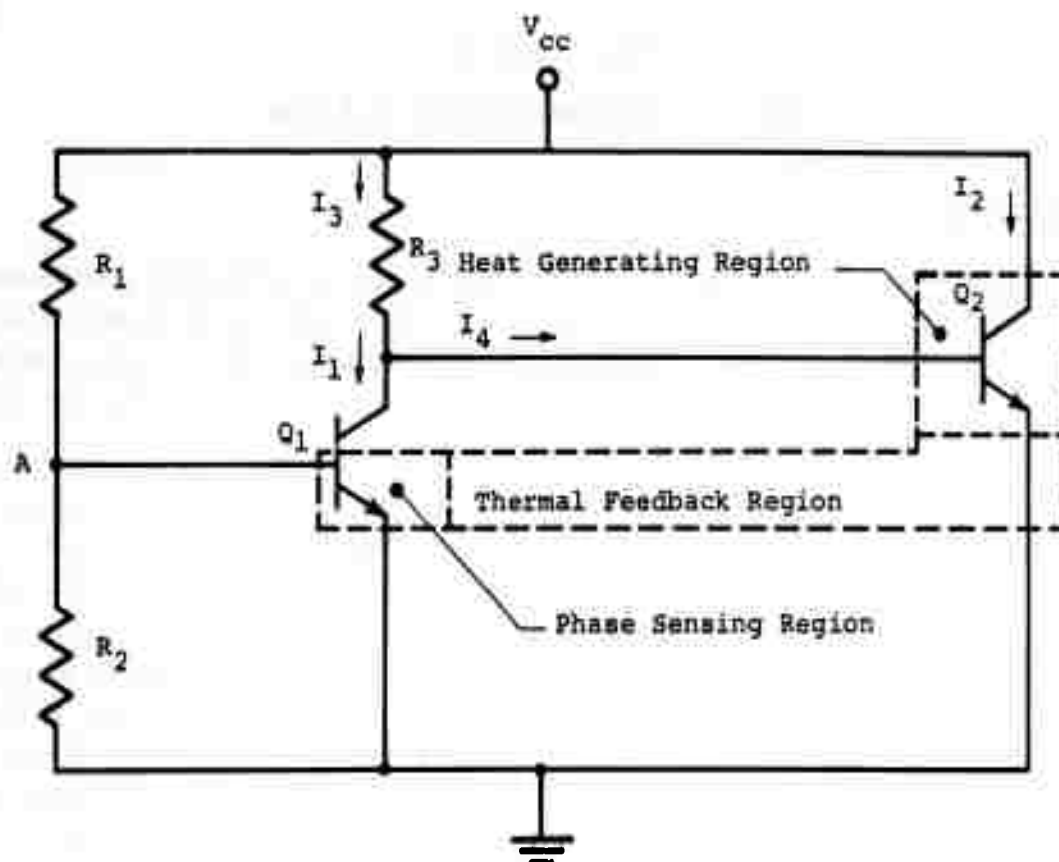


Figure 33. Integrated Circuit Low Frequency Oscillator

region at a constant temperature. If the ambient temperature increases, the temperature of the  $Q_1$  base-emitter region will increase, and the collector current  $I_1$  increases. This reduces the current to the base of  $Q_2$ .  $Q_2$  then provides less heat to  $Q_1$  and the temperature tends to decrease to the previously established equilibrium value. Using the same reasoning, temperature decreases are also counteracted. This circuit appears to be a simple method of controlling the temperature of an integrated circuit substrate, but it is a feedback system with the feedback provided by the thermal coupling between  $Q_2$  and  $Q_1$ . As previously explained the feedback is negative, but there is a finite time delay associated with heat flow and the feedback may also be positive. If certain requirements on gain and feedback ratio are satisfied, the amplifier will be unstable and oscillate.

The electrical circuit analog of thermal conduction is current flow through a transmission line made up of series resistance and distributed shunt capacitance. Heat flow and temperature correspond to current flow and voltage respectively. The time delay between a change in heating effect at  $Q_2$  and its detection as a change in temperature at  $Q_1$  can also be considered in terms of  $Q_1$  detecting a change in phase shift and attenuation of a thermal wave propagating outward from  $Q_2$ . This is identical to considering an electrical transmission line from either the time delay or phase shift point of view. When considered in terms of phase shift, thermal oscillation should result when the phase of the thermal value is shifted by 180 degrees, provided the electrical gain of the amplifier overcomes all the thermal losses.

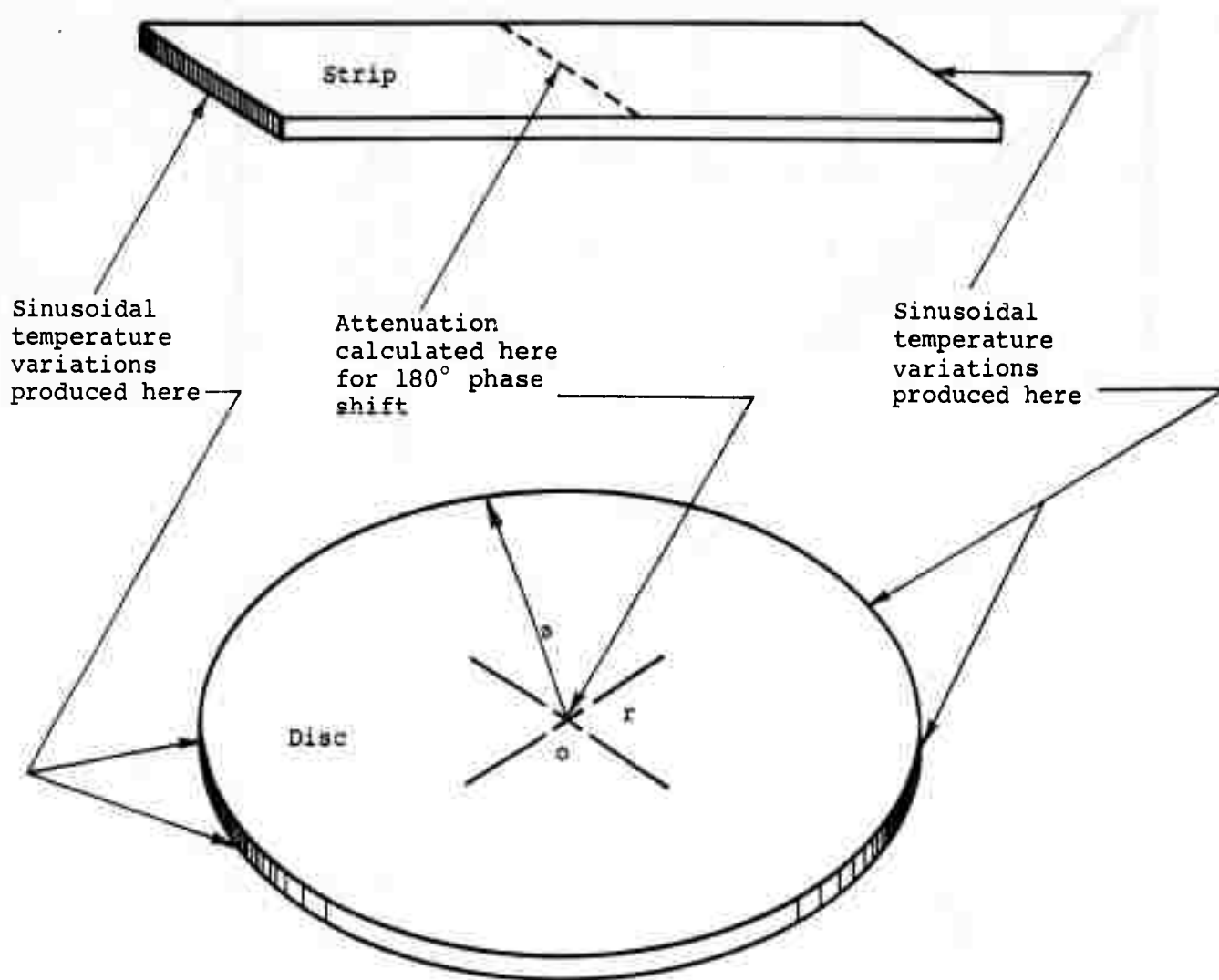


Figure 34. Geometrical Configurations for Thermal Element

Phase shift and attenuation of thermal waves are determined by the geometry of the conduction path and the physical constants of the conduction medium. These constants are density, thermal conductivity, and specific heat. Since the phase shift and frequency are related, the frequency of oscillation is also determined by the geometry and thermal characteristics of the feedback circuitry.

Prior to this contract, calculations of the thermal phase shift and attenuation were made for two simple geometrical configurations. Specifically the attenuation for a phase shift of 180 degrees was desired, since this determines the gain necessary for oscillation. The electrical gain must offset this thermal attenuation and any losses involved in converting an electrical signal to a thermal signal and then back to an electrical signal. The results of these calculations are given in the proposal Advanced Functional Electronic Block Development which resulted from Request for Proposal NR 33(657)-62-5747-Q.

This previous work was extended during this report period. Calculations were made for two additional configurations. One was the thin rectangular strip shown in Figure 34. Sinusoidal temperature variations were assumed

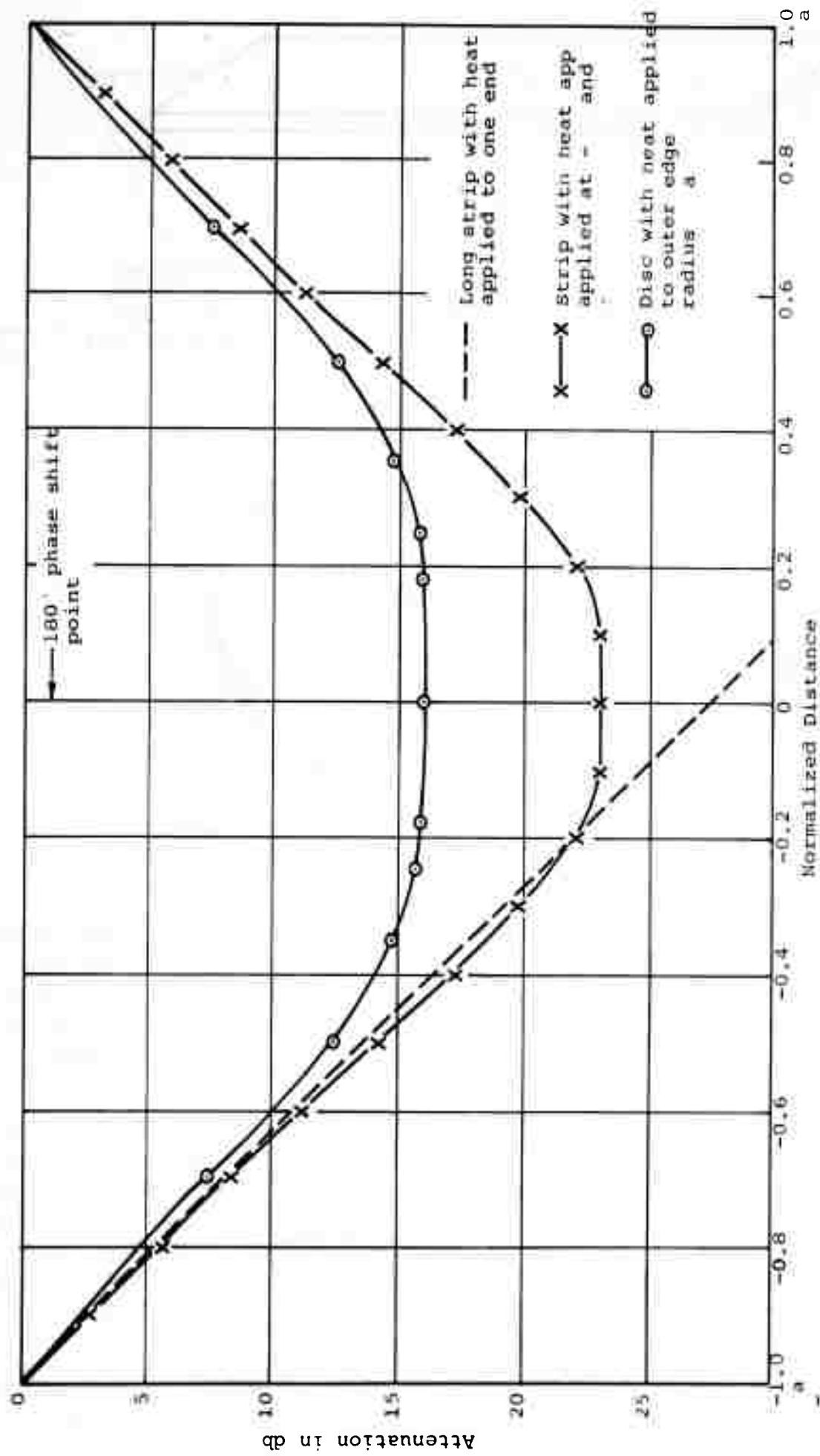


Figure 35. Attenuation Versus Normalized Distance

at the two ends. The thermal phase shift and attenuation were calculated at a point equidistant from the ends. The other configuration was a thin disc, also shown in Figure 34. In this case the outer rim was assumed thermally excited and the phase shift and attenuation calculated at the center. In each case the important result was the calculation of the attenuation of the thermal wave when the phase had been shifted by 180 degrees. The attenuation at this point for a long rectangular strip excited at only one end is  $1/23.3$ , while for the presently considered strip and disc the attenuations are  $1/11.8$  and  $1/6.34$  respectively. Either of these two configurations has less thermal attenuation than those previously calculated, and would appear to be more desirable as oscillators.

The attenuation versus distance for both configurations is given in Figure 35. In both cases the position axis is normalized for 180 degree phase shift at the midpoint. A plot of a long thin bar excited at one end is included as a reference. Figure 36 shows phase shift with position. Both the attenuation and phase shift plots indicate that the location of a sensing element is not too critical in the region around the center, since the slope of each curve is small.

At this time the circular disc appears to be the most advantageous with respect to thermal attenuation, but other factors should be considered. The efficiency with respect to power may not be optimum for this configuration. Also a thermal shunting effect which results from mounting the disc will affect the thermal oscillator.

### C. PLANS

Analysis of the circular disc configuration will be continued. The methods for generating and detecting thermal waves which can be used in semiconductor networks will also be investigated. The literature search for applicable thermoelectric effects will be continued.

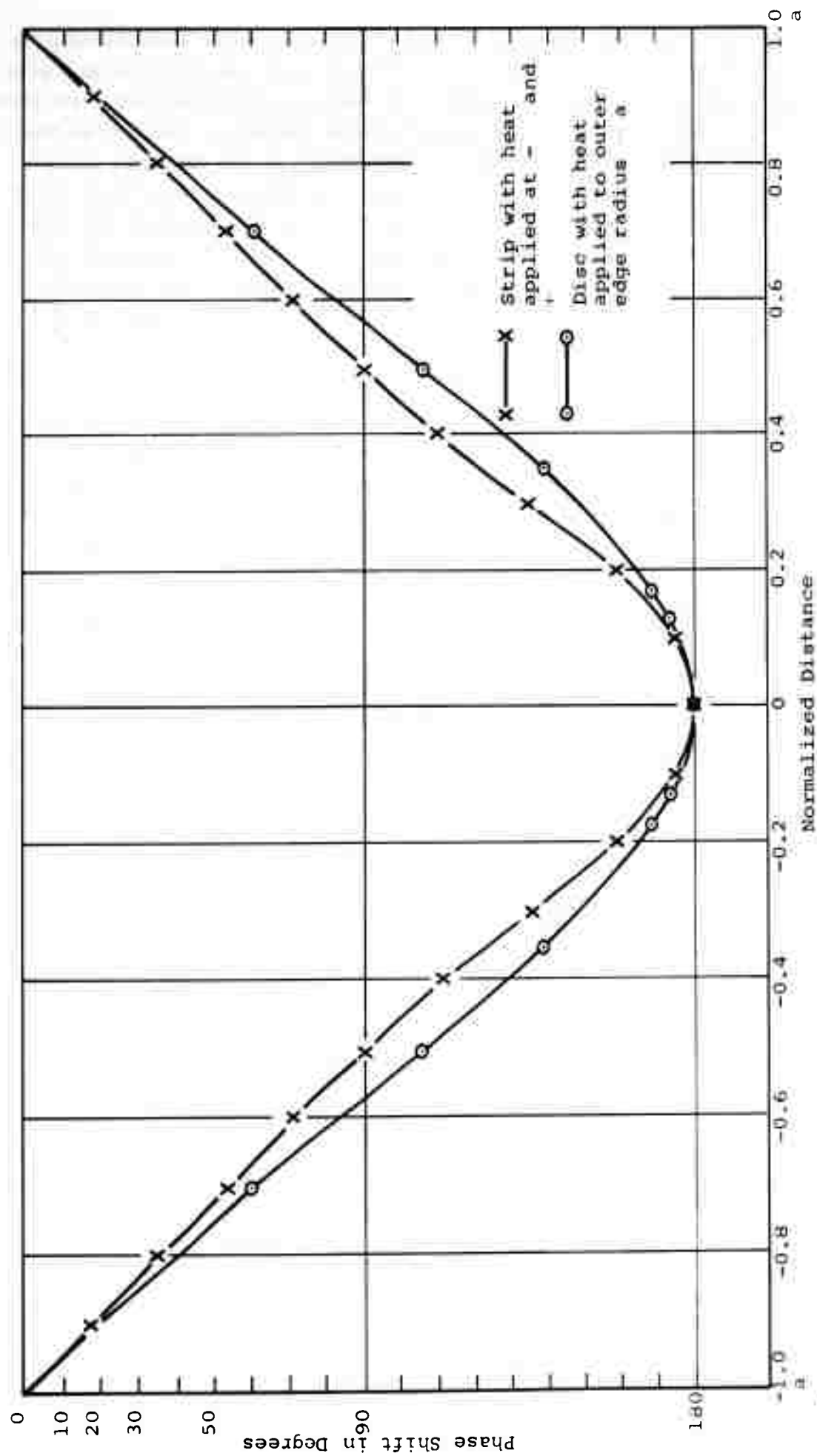


Figure 36. Phase Shift Versus Normalized Distance

## BIBLIOGRAPHY

1. R. N. Hall, "Recombination Processes in Semiconductors," Proc. of IEE Vol. 107 (March 1960), pp. 923-931.
2. G. Burns, A. E. Michel, and M. I. Nathan, "Electroluminescent GaAs Diodes," Electron Devices Meeting, October 25-27, 1962, Washington, D. C.
3. J. R. Biard, E. L. Bonin, W. N. Carr, and G. E. Pittman, "A GaAs Source for Infrared Applications," Electron Devices Meeting, October 25-27, 1962, Washington, D. C.
4. C. T. Sah, R. N. Noyce, and W. Shockley, "Carrier Generation and Recombination in P-N Junctions and P-N Junction Characteristics," Proc. of the IRE, Vol. 45, September 1957.
5. P. J. Coppen and W. T. Matzen, "Distribution of Recombination Current in Emitter-Base Junctions of Silicon Transistors," Trans. of the PGED, Vol. ED-9, January 1962.
6. L. J. Vieland, "Behavior of Mn in GaAs," Journal of Applied Physics, Vol. 33 (June 1962), pp. 2007-2008.
7. D. N. Nasledov, et. al., "Recombination Radiation of GaAs," Soviet Physics-Solid State (Corres), Vol. 4 (October 1962), p. 782.
8. J. I. Pankove and M. Massonlie, "Recombination Radiation in GaAs P-N Junction," J. Electrochem. Soc., Vol. 11 (1962), pp. 71-75.
9. R. J. Keyes and T. M. Quist, "Recombination Radiation Emitted by GaAs," Proc. of the IRE (Corres), Vol. 50 (August 1962), pp. 1822-23.
10. R. N. Hall, G. E. Fenner, J. D. Kingsley, T. J. Soltys, and R. O. Carlson, "Coherent Light Emission From GaAs Junctions," Phys. Rev. Letters, Vol. 9 (November 1, 1962), pp. 366-368.
11. M. I. Nathan, W. P. Dumke, G. Burns, F. H. Dill, Jr., and G. Lasher, "Stimulated Emission of Radiation From GaAs P-N Junctions," Applied Phys. Letters, Vol. 1 (November 1, 1962), pp. 62-64.
12. T. M. Quist, R. J. Keyes, W. E. Krag, B. Lax, A. L. McWhorter, R. H. Rediker, and H. J. Zieger, "Semiconductor Maser in GaAs," to be published in Appl. Phys. Letters.
13. H. J. Zeiger and W. E. Krag, "Semiconductor Infrared Maser Studies," Quarterly Solid-State Progress Report, Lincoln Laboratory, Lexington, Massachusetts, October 15, 1959.
14. N. G. Basov, O. N. Krokhin, and Ju. M. Popov, "Negative Absorption Coefficient at Indirect Transitions in Semiconductors," Second Intl. Conf. on Quantum Electronics, Berkeley, California, March 23-25, 1961.



15. M. G. Bernard and G. Duraffourg, "Laser Conditions in Semiconductors," Physica Status Solidi, 1 (November 1961), pp. 699-703.
16. E. I. Adirovich, E. M. Kuznetsova, "Possible Inverted Distribution of Electrons in Degenerate Semiconductors," Soviet Physics-Solid State, Vol. 4, May 1962.
17. W. P. Dumke, "Interband Transitions and Maser Action," Phys. Review, Vol. 127 (September 1, 1962), pp. 1559-1563.
18. O. N. Krokhin, "Negative Absorption Associated With Indirect Exciton Recombination in Semiconductors," Soviet Physics-Solid State (Corres), Vol. 4 (September 1962), pp. 604-606.
19. W. S. Boyle and D. G. Thomas, US Patent 3059117, October 16, 1962.
20. D. G. Thomas and J. J. Hopfield, "Fluorescence in CdS and Its Possible Use for an Optical Laser," Jour. Appl. Phys., Vol. 33 (November 1962), pp. 3243-3249.
21. G. Burns and M. I. Nathan, to be published in Phys. Rev.
22. R. W. Smith, "Ohmic Contacts to CdS Single Crystals," Phys. Rev. Vol. 97 (1955), p. 1525.
23. Richard H. Bube, Photoconductivity of Solids (John Wiley and Sons, Inc., 1960), pp. 118-119.
24. K. W. Boer and K. Lubitz, "Zum Kontakproblem on CdS-Einkristallen," Zietschrift fur Naturforschung, 17a (1962), pp. 397-405.
25. R. A. Griener, R. F. Miller, and R. C. Retherford, "Effect of Electrode Materials and Surface Preparation on CdS-Metal Contacts," Jour. Appl. Physics, Vol. 28 (1957), p. 1358.
26. Richard H. Bube, Photoconductivity of Solids (John Wiley and Sons, Inc., 1960), pp. 175, 187-188.
27. J. A. Beun, R. Nitsche, and Bolsterli, "After Treatment of CdS Single Crystals Grown by Vapour Transport with I<sub>2</sub>," Physica 28 (1962), p. 184.
28. F. A. Kroger, H. J. Vink, and J. Boongaard, "Controlled Conductivity of CdS Single Crystals," Zeitschrift fur Physikalische Chemie 202 (1954), p. 1.
29. R. H. Fahrig, K. E. Bean, J. E. Powderly, S. J. Roderique, and W. E. Medcalf, "Research in Purification of CdS Crystals," Contract AF33(616)-6203, Project 7116, Task 70715 (April 1961), pp. 21-25.
30. M. Aver and H. H. Woodbury, "Investigation of Semiconducting Properties of the II-VI Compounds," Contract No. AF19(604)-3512, Project 4608, Task 46088, June 1962.

<p>Aeronautical Systems Division, /Dir Avionics, Wright-Patterson AFB, Ohio Rpt. Nr ASD-TDR-63-----ADVANCED FUNCTIONAL ELECTRONIC BLOCK DEVELOPMENT. First Interim Report April 1963, 57 p, incl illus, tables, 30 refs.</p> <p>Unclassified Report</p> <p>This report describes investigations of new semiconductor phenomena for application in Advanced Functional Electronic Blocks. The work is divided into four specific tasks as follows:</p> <p>Task I. GaAs Emission Technology - Optical and electrical characteristics of both spontaneous emission sources and lasers are presented. A discussion of possible radiative recombination mechanisms is included.</p>	<p>UNCLASSIFIED</p> <ol style="list-style-type: none"> <li>1. Semiconductor Devices</li> <li>2. Molecular Electronics</li> <li>3. Packaged Circuits</li> <li>4. Microminiaturization</li> </ol> <ol style="list-style-type: none"> <li>I. AFSC Project 4159 Task 415906</li> <li>II. Contract No. AF33(657)-9824</li> <li>III. Texas Instruments Incorporated, Dallas, Texas</li> <li>IV. Author, J. R. Biard</li> </ol> <p>UNCLASSIFIED</p>
--	--

<p>Aeronautical Systems Division, /Dir Avionics, Wright-Patterson AFB, Ohio Rpt. Nr ASD-TDR-63-----ADVANCED FUNCTIONAL ELECTRONIC BLOCK DEVELOPMENT. First Interim Report April 1963, 57 p, incl illus, tables, 30 refs.</p> <p>Unclassified Report</p> <p>This report describes investigations of new semiconductor phenomena for application in Advanced Functional Electronic Blocks. The work is divided into four specific tasks as follows:</p> <p>Task I. GaAs Emission Technology - Optical and electrical characteristics of both spontaneous emission sources and lasers are presented. A discussion of possible radiative recombination mechanisms is included.</p>	<p>UNCLASSIFIED</p> <ol style="list-style-type: none"> <li>1. Semiconductor Devices</li> <li>2. Molecular Electronics</li> <li>3. Packaged Circuits</li> <li>4. Microminiaturization</li> </ol> <ol style="list-style-type: none"> <li>I. AFSC Project 4159 Task 415906</li> <li>II. Contract No. AF33(657)-9824</li> <li>III. Texas Instruments Incorporated, Dallas, Texas</li> <li>IV. Author, J. R. Biard</li> </ol> <p>UNCLASSIFIED</p>
--	--

Task II. Light Multiplexing - A low-level photodetector has been selected as the first application of the GaAs IR source to FEB's. Techniques to improve optical coupling between the source and silicon photodetector are described.

Task III. Acoustic Amplifier - This task is an exploratory investigation of the Ultrasonic Amplification effect in piezoelectric semiconductors. Test facility, fabrication techniques and experimental results are described for Cds amplifiers.

Task IV. Thermal Oscillator - Electrical and geometrical design for a thermal low-frequency oscillator in semiconductor network form is described.

Task II. Light Multiplexing - A low-level photodetector has been selected as the first application of the GaAs IR source to FEB's. Techniques to improve optical coupling between the source and silicon photodetector are described.

Task III. Acoustic Amplifier - This task is an exploratory investigation of the Ultrasonic Amplification effect in piezoelectric semiconductors. Test facility, fabrication techniques and experimental results are described for Cds amplifiers.

Task IV. Thermal Oscillator - Electrical and geometrical design for a thermal low-frequency oscillator in semiconductor network form is described.

<p>Aeronautical Systems Division, /Dir Avionics, Wright-Patterson AFB, Ohio Rpt. Nr ASD-TDR-63-ADVANCED FUNCTIONAL ELECTRONIC BLOCK DEVELOPMENT. First Interim Report April 1963, 57 p, incl illus, tables, 30 refs. Unclassified Report</p>	<p>UNCLASSIFIED</p> <ol style="list-style-type: none"> <li>1. Semiconductor Devices</li> <li>2. Semiconductor Electronics</li> <li>3. Molecular Electronics</li> <li>4. Packaged Circuits</li> <li>5. Microminiaturization</li> </ol> <p>I. AFSC Project 4159 Task 415906 II. Contract No. AF33(657)-9824 III. Texas Instruments Incorporated, Dallas, Texas IV. Author, J. R. Biard</p>	<p>UNCLASSIFIED</p>
<p>Aeronautical Systems Division, /Dir Avionics, Wright-Patterson AFB, Ohio Rpt. Nr ASD-TDR-63-ADVANCED FUNCTIONAL ELECTRONIC BLOCK DEVELOPMENT. First Interim Report April 1963, 57 p, incl illus, tables, 30 refs. Unclassified Report</p>	<p>UNCLASSIFIED</p> <ol style="list-style-type: none"> <li>1. Semiconductor Devices</li> <li>2. Semiconductor Electronics</li> <li>3. Molecular Electronics</li> <li>4. Packaged Circuits</li> <li>5. Microminiaturization</li> </ol> <p>I. AFSC Project 4159 Task 415906 II. Contract No. AF33(657)-9824 III. Texas Instruments Incorporated, Dallas, Texas IV. Author, J. R. Biard</p>	<p>UNCLASSIFIED</p>
<p>Task II. Light Multiplexing - A low-level photochopper has been selected as the first application of the GaAs IR source to FEB's. Techniques to improve optical coupling between the source and silicon photodetector are described.</p> <p>Task III. Acoustic Amplifier - This task is an exploratory investigation of the Ultrasonic Amplification effect in piezoelectric semiconductors. Test facility, fabrication techniques and experimental results are described for CdS amplifiers.</p> <p>Task IV. Thermal Oscillator - Electrical and geometrical design for a thermal low-frequency oscillator in semiconductor network form is described.</p>	<p>Task II. Light Multiplexing - A low-level photochopper has been selected as the first application of the GaAs IR source to FEB's. Techniques to improve optical coupling between the source and silicon photodetector are described.</p> <p>Task III. Acoustic Amplifier - This task is an exploratory investigation of the Ultrasonic Amplification effect in piezoelectric semiconductors. Test facility, fabrication techniques and experimental results are described for CdS amplifiers.</p> <p>Task IV. Thermal Oscillator - Electrical and geometrical design for a thermal low-frequency oscillator in semiconductor network form is described.</p>	<p>UNCLASSIFIED</p>
<p>Task II. Light Multiplexing - A low-level photochopper has been selected as the first application of the GaAs IR source to FEB's. Techniques to improve optical coupling between the source and silicon photodetector are described.</p> <p>Task III. Acoustic Amplifier - This task is an exploratory investigation of the Ultrasonic Amplification effect in piezoelectric semiconductors. Test facility, fabrication techniques and experimental results are described for CdS amplifiers.</p> <p>Task IV. Thermal Oscillator - Electrical and geometrical design for a thermal low-frequency oscillator in semiconductor network form is described.</p>	<p>Task II. Light Multiplexing - A low-level photochopper has been selected as the first application of the GaAs IR source to FEB's. Techniques to improve optical coupling between the source and silicon photodetector are described.</p> <p>Task III. Acoustic Amplifier - This task is an exploratory investigation of the Ultrasonic Amplification effect in piezoelectric semiconductors. Test facility, fabrication techniques and experimental results are described for CdS amplifiers.</p> <p>Task IV. Thermal Oscillator - Electrical and geometrical design for a thermal low-frequency oscillator in semiconductor network form is described.</p>	<p>UNCLASSIFIED</p>

Aeronautical Systems Division, /Dir Avionics,  
Wright-Patterson AFB, Ohio  
Rpt. No. ASD-TDR-63-ADVANCED FUNCTIONAL ELECTRONIC BLOCK DEVELOPMENT.  
First Interim Report April 1963, 57 p. incl  
illus, tables, 30 refs.

Unclassified Report

This report describes investigations of new semiconductor phenomena for application in Advanced Functional Electronic Blocks. The work is divided into four specific tasks as follows:

Task I. GaAs Emission Technology - Optical and electrical characteristics of both spontaneous emission sources and lasers are presented. A discussion of possible radiative recombination mechanisms is included.

Task II. Light Multiplexing - A low-level photochopper has been selected as the first application of the GaAs IR source to FEB's. Techniques to improve optical coupling between the source and silicon photodetector are described.

Task III. Acoustic Amplifier - This task is an exploratory investigation of the Ultrasonic Amplification effect in piezoelectric semiconductors. Test facility, fabrication techniques and experimental results are described for CdS amplifiers.

Task IV. Thermal Oscillator - Electrical and geometrical design for a thermal low-frequency oscillator in semiconductor network form is described.

#### UNCLASSIFIED

1. Semiconductors
2. Semiconductor Devices
3. Molecular Electronics
4. Packaged Circuits
5. Microminiaturization

I. AFSC Project 4159

Task 415906

II. Contract No.

AF33(657)-9824

III. Texas Instruments

Incorporated,

Dallas, Texas

IV. Author, J. R. Biard

UNCLASSIFIED

Aeronautical Systems Division, /Dir Avionics,  
Wright-Patterson AFB, Ohio  
Rpt. No. ASD-TDR-63-ADVANCED FUNCTIONAL ELECTRONIC BLOCK DEVELOPMENT.  
First Interim Report April 1963, 57 p. incl  
illus, tables, 30 refs.

Unclassified Report

This report describes investigations of new semiconductor phenomena for application in Advanced Functional Electronic Blocks. The work is divided into four specific tasks as follows:

Task I. GaAs Emission Technology - Optical and electrical characteristics of both spontaneous emission sources and lasers are presented. A discussion of possible radiative recombination mechanisms is included.

Task II. Light Multiplexing - A low-level photochopper has been selected as the first application of the GaAs IR source to FEB's. Techniques to improve optical coupling between the source and silicon photodetector are described.

Task III. Acoustic Amplifier - This task is an exploratory investigation of the Ultrasonic Amplification effect in piezoelectric semiconductors. Test facility, fabrication techniques and experimental results are described for CdS amplifiers.

Task IV. Thermal Oscillator - Electrical and geometrical design for a thermal low-frequency oscillator in semiconductor network form is described.

#### UNCLASSIFIED

1. Semiconductors
2. Semiconductor Devices
3. Molecular Electronics
4. Packaged Circuits
5. Microminiaturization

I. AFSC Project 4159

Task 415906

II. Contract No.

AF33(657)-9824

III. Texas Instruments

Incorporated,

Dallas, Texas

IV. Author, J. R. Biard

UNCLASSIFIED

Aeronautical Systems Division, /Dir Avionics,  
Wright-Patterson AFB, Ohio

Rpt. Nr ASD-TDR-63-ADVANCED FUNCTIONAL ELECTRONIC BLOCK DEVELOPMENT.

First Interim Report April 1963, 57 p, incl  
illus, tables, 30 refs.

Unclassified Report

This report describes investigations of new semiconductor phenomena for application in Advanced Functional Electronic Blocks. The work is divided into four specific tasks as follows:

Task I. GaAs Emission Technology - Optical and electrical characteristics of both spontaneous emission sources and lasers are presented. A discussion of possible radiative recombination mechanisms is included.

UNCLASSIFIED

1. Semiconductors
2. Semiconductor Devices
3. Molecular Electronics
4. Packaged Circuits
5. Microminiaturization

I. AFSC Project 4159

Task 415906

II. Contract No.

AF33(657)-9824

III. Texas Instruments

Incorporated,

Dallas, Texas

IV. Author, J. R. Biard

UNCLASSIFIED

Task II. Light Multiplexing - A low-level photochopper has been selected as the first application of the GaAs IR source to FEB's. Techniques to improve optical coupling between the source and silicon photodetector are described.

Task III. Acoustic Amplifier - This task is an exploratory investigation of the Ultrasonic Amplification effect in piezoelectric semiconductors. Test facility, fabrication techniques and experimental results are described for CdS amplifiers.

Task IV. Thermal Oscillator - Electrical and geometrical design for a thermal low-frequency oscillator in semiconductor network form is described.

Aeronautical Systems Division, /Dir Avionics,  
Wright-Patterson AFB, Ohio

Rpt. Nr ASD-TDR-63-ADVANCED FUNCTIONAL ELECTRONIC BLOCK DEVELOPMENT.

First Interim Report April 1963, 57 p, incl  
illus, tables, 30 refs.

Unclassified Report

This report describes investigations of new semiconductor phenomena for application in Advanced Functional Electronic Blocks. The work is divided into four specific tasks as follows:

Task I. GaAs Emission Technology - Optical and electrical characteristics of both spontaneous emission sources and lasers are presented. A discussion of possible radiative recombination mechanisms is included.

UNCLASSIFIED

UNCLASSIFIED

1. Semiconductors
2. Semiconductor Devices
3. Molecular Electronics
4. Packaged Circuits
5. Microminiaturization

I. AFSC Project 4159

Task 415906

II. Contract No.

AF33(657)-9824

III. Texas Instruments

Incorporated,

Dallas, Texas

IV. Author, J. R. Biard

UNCLASSIFIED

UNCLASSIFIED